2D Materials

ACCEPTED MANUSCRIPT • OPEN ACCESS

Monolayer WS_2 electro- and photo-luminescence enhancement by TFSI treatment

To cite this article before publication: Alisson Cadore *et al* 2024 *2D Mater.* in press https://doi.org/10.1088/2053-1583/ad1a6a

Manuscript version: Accepted Manuscript

Accepted Manuscript is “the version of the article accepted for publication including all changes made as a result of the peer review process, and which may also include the addition to the article by IOP Publishing of a header, an article ID, a cover sheet and/or an ‘Accepted Manuscript’ watermark, but excluding any other editing, typesetting or other changes made by IOP Publishing and/or its licensors”

This Accepted Manuscript is **© 2024 The Author(s). Published by IOP Publishing Ltd**.

As the Version of Record of this article is going to be / has been published on a gold open access basis under a CC BY 4.0 licence, this Accepted Manuscript is available for reuse under a CC BY 4.0 licence immediately.

Everyone is permitted to use all or part of the original content in this article, provided that they adhere to all the terms of the licence https://creativecommons.org/licences/by/4.0

Although reasonable endeavours have been taken to obtain all necessary permissions from third parties to include their copyrighted content within this article, their full citation and copyright line may not be present in this Accepted Manuscript version. Before using any content from this article, please refer to the Version of Record on IOPscience once published for full citation and copyright details, as permissions may be required. All third party content is fully copyright protected and is not published on a gold open access basis under a CC BY licence, unless that is specifically stated in the figure caption in the Version of Record.

View the article online for updates and enhancements.

This content was downloaded from IP address 131.111.184.3 on 25/01/2024 at 10:54

Monolayer WS_2 electro- and photo-luminescence enhancement by TFSI treatment

A. R. Cadore[1],* B. L. T. Rosa[1], I. Paradisanos[1], S. Mignuzzi[1], D. De Fazio[1], E. M. Alexeev[1], A. Dagkli[2], J. E. Muench[1], G. Kakavelakis[1], S. M. Shinde[1], D. Yoon[1], S. Tongay[3], K. Watanabe[4], T. Taniguchi[4], E. Lidorikis[2], I. Goykhman[1],† G. Soavi[1],‡ and A. C. Ferrari[1]§

[1]*Cambridge Graphene Centre, University of Cambridge, Cambridge CB3 0FA, UK*

[2]*Department of Materials Science and Engineering, University of Ioannina, Ioannina, Greece*

[3]*School for Engineering of Matter, Transport and Energy, Arizona State University, Tempe, USA and*

[4]*Advanced Materials Laboratory, 1-1 Namiki, Tsukuba, Japan*

Layered material heterostructures (LMHs) can be used to fabricate electroluminescent devices operating in the visible spectral region. A major advantage of LMH-light emitting diodes (LEDs) is that electroluminescence (EL) emission can be tuned across that of different exciton complexes (e.g. biexcitons, trions, quintons) by controlling the charge density. However, these devices have an EL quantum efficiency as low as$\sim 10^{-4}$%. Here, we show that the superacid bis-(trifluoromethane)sulfonimide (TFSI) treatment of monolayer WS_2-LEDs boosts EL quantum efficiency by over one order of magnitude at room temperature. Non-treated devices emit light mainly from negatively charged excitons, while the emission in treated ones predominantly involves radiative recombination of neutral excitons. This paves the way to tunable and efficient LMH-LEDs.

Transition metal dichalcogenide monolayers (1L-TMDs) are ideal to study light-matter interactions and many-body effects at the atomic scale[1–3]. Compared to bulk semiconductors[2], the reduced dielectric screening combined with the spatial confinement of charge carriers[1] favours the formation of various excitonic complexes which can be controlled by modulation of the carrier density[1–8]. Thus, 1L-TMDs photoluminescence (PL) spectra host features arising from formation of charged[4–8] and neutral[9–12] exciton complexes.

Layered material heterostructures (LMHs) combining single layer graphene (SLG), 1L-TMDs, and hexagonal boron nitride (hBN), from 1L-hBN to hundreds of layers, are promising for electronics[13, 14], photonics[15], and optoelectronics[16, 17]. Direct bandgap 1L-TMDs and LMHs can be used to make light-emitting diodes (LEDs)[18–27], with fast modulation speed (up to GHz)[7, 25, 28], and emission wavelength tunability[6, 7, 25] besides multi-spectral (visible$\sim$618nm[21–23] to near-infrared$\sim$1160nm[29, 30]) emission.

In 1L-TMD-based LEDs, the electroluminescence (EL) efficiency (η_{EL}), i.e. ratio between emitted photons and injected electrons (e)[19, 20], depends on the optical emission of the material[30–37], as well as on its doping level[6, 38–41]. In doped 1L-TMDs, the PL and EL emission originates from either negative (X^-)[28, 33, 34, 38] or positive (X^+)[6, 19, 20] trions, depending on the type of doping. However, 1L-TMD-LEDs based on trionic emission show low η_{EL} (typically$<$0.05%[19, 20]) with respect to neutral exciton (X^0) emission (typically $\eta_{EL}<1$%[6, 7, 31, 32, 38, 39]). This difference in η_{EL} occurs due the small ($\sim$30meV) binding energy of trions[42]. Since the X^- binding energy is close to the lattice thermal energy at room-temperature (RT=300K,$\sim$25.2meV), trions dissociate[2]. An excess of free-carriers decreases the available phase-space filling for exciton complexes, due to Pauli blocking, with a reduction of trion and exciton binding energies[43] and oscillator strengths[44] (i.e. the probability of absorption/emission of electromagnetic radiation[45]).

In 1L-TMDs, low light-emission efficiency is observed in both EL (η_{EL} $\sim 10^{-4}$[33, 34] to$\sim$1%[6, 7, 31, 32, 38, 39]) and PL (η_{PL} $\sim 10^{-3}$[36, 40] to$\sim$5%[1–3]). η_{PL} is defined as the ratio between emitted and absorbed photons[19, 20]. Thus, several chemical approaches were suggested[46] to enhance η_{PL}, such as treatment with sodium sulphide[47], 2,3,5,6 tetrafluoro tetracyanoquinodimethane (F4TCNQ)[11, 48], tris(4-bromophenyl)ammoniumyl hexachloroantimonate (magic blue)[49], water[11], hydrogen peroxide[50], titanyl phthalocyanine[51], sulfuric acid[52], oleic acid[53–55], and the superacid (i.e. with acidity greater than that of 100% pure sulfuric acid[56]) bis-(trifluoromethane)sulfonimide (TFSI)[49, 57–70], in addition to other no chemical treatments[8, 71–75]. The PL enhancement reported to date for 1L-WS2 treated with different chemical and non-chemical approaches is summarized in Table 1. The effect of chemical passivation of on η_{EL} combined with gated-PL emission in 1L-TMD-based LEDs was not reported to date, to the best of our knowledge.

Refs.[57–64] reported PL measurements on 1L-TMDs and focused on non-gated samples, thus limiting the modulation of charge density in 1L-TMDs. Ref.[8] performed gated-PL measurements in 1L-WS_2, finding that both TFSI treatment and electrical gating increase η_{PL} by a factor of up to$\sim$10 (at$\sim 10^{19}$cm^{-2}s^{-1} photocarrier generation rate), because both processes reduce the n-type behaviour of 1L-WS_2 and suppress X^- formation, thus enhancing X^0 radiative recombination. However, gated-PL measurements after TFSI passivation were not provided. The activation of trapping states on TFSI-treated 1L-TMDs was not discussed. Ref.[76] carried out EL experiments with TFSI passivation for high-speed

Accepted Manuscript

TABLE I. PL and EL intensity enhancement for 1L-WS_2 treated with different methods compared to pristine samples. The PL and EL intensities of pristine samples is normalized to 1. X means no value reported

	Relative PL intensity enhancement	Relative EL intensity enhancement	Reference
Chemical Methods			
Sodium Triflanate	∼1 times	X	[49]
Lithium Triflate	∼2 times	X	[49]
Water	1 to 4 times	X	[11]
F4TCNQ	1 to 5 times	X	[11, 49]
TFSI	1 to 11 times	X	[55, 57, 59, 60, 69, 70]
TFSI	∼5 times	∼5 times	[76]
TFSI	∼5 times	∼10 times	This work
Magic blue	∼9 times	X	[49]
Sodium Sulphide	5 to 25 times	X	[47]
Oleic Acid	10 to 26 times	X	[53–55]
Non-Chemical Methods			
Pulsed V bias	X	∼4 times	[33]
Plasmonic Ag Nanowires	∼4-7 times	X	[72]
Ag film	∼10 times	X	[74]
Au nanoantenna	4 to 10 times	X	[75]
Photonic cavity	X	up to 16 times	This work

(MHz) modulation, but did not report PL nor EL emission tunability. Therefore, an investigation on how TFSI affects EL emission and modifies gated-PL of 1L-TMD-based devices is required.

Here, we fabricate LEDs with 1L-WS_2 as active material on a metal-insulator-semiconductor (MIS) structure. We measure EL and gated-PL before and after TFSI treatment. We find that TFSI increases η_{EL} by over one order of magnitude at RT, and PL intensity by a factor∼5. Our PL results on TFSI-treated samples agree with previous literature, Table 1[57, 59, 60, 69, 70], while EL for TFSI-treated samples is twice than of Ref.[76], reporting both EL and PL characterization before and after TFSI treatment, but not gated-PL. We find that X^- and X^0 are present in both EL and PL before TFSI treatment, whereas X^0 dominates after. We attribute this to depletion of excess e and changes in the relaxation pathway, induced by the treatment. This paves the way to more efficient 1L-TMDs-based LEDs and excitonic devices.

RESULTS AND DISCUSSION

We use 1L-WS_2 as the active light-emitting layer since it has a direct bandgap[77–80], its PL emission is∼60 times stronger than 1L-MoS_2[39, 78] at RT, η_{EL} can be up to∼50 times larger than 1L-MoS_2[19, 20] at RT, while Refs.[55, 57–68] demonstrated that TFSI treatment increases up to∼10-times its PL intensity.

Fig.1a shows the 1L-WS_2/hBN/SLG tunnel junction configuration used here, where the metallic electrodes provide contacts to apply a voltage (V) between SLG and 1L-WS_2. This is prepared as follows.

WS_2 crystals are synthesized using a two-step self-flux technique[81] using 99.9999% purity W and S powders without any transporting agents. Commercial (Alfa Aesar) sources of powders contain a number of defects and impurities (Li, O, Na, and other metals as determined by secondary ion mass spectroscopy). Before growth, W and S powders are thus purified using electrolytic[82] and H_2[82] based techniques to reach 99.995% purity. WS_2 polycrystalline powders are created by annealing a stoichiometric ratio of powders at 900°C for 3 weeks in a quartz ampoule sealed at 10^{-7} Torr. The resulting powders are re-sealed in a different quartz ampoule under similar pressures and further annealed at 870-910°C with thermodynamic temperature differential (hot to cold zone difference)∼40°C. The growth process takes 5 weeks. At the end of the growth, ampoules are cooled to RT slowly (∼40°C/hour)[83]. We use this material as bulk source because we previously[83] demonstrated that this has a point defect density∼10^9-10^{10} cm^{-2}, on par or better than previous reports[84].

Bulk WS_2, hBN (grown by the temperature-gradient method[85]), and graphite (sourced from HQ Graphene) crystals are then exfoliated by micromechanical cleavage using Nitto-tape[86] on 285nm SiO_2/Si. Optical contrast[87] is first used to identify 1L-WS_2, SLG, FLG (3-10nm), and hBN(<5nm). The LMs are then charac-

Accepted Manuscript

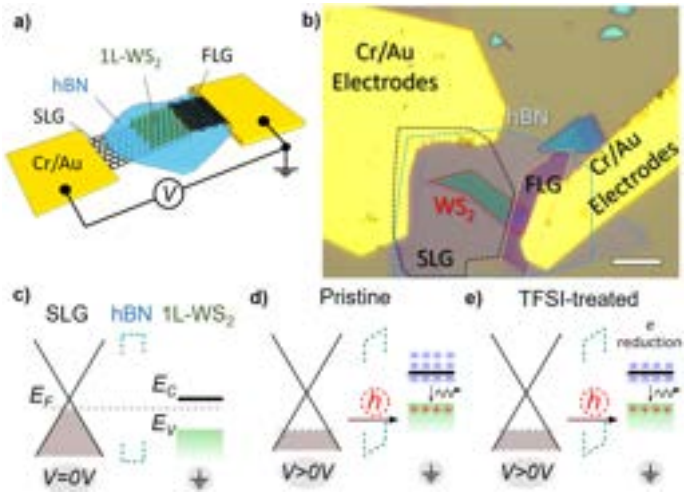

FIG. 1. a) Schematic of LED. Cr/Au electrodes, SLG, FLG, hBN, and 1L-WS_2 are indicated as well as the electrical connection. b) Optical image of device. Scale bar 4μm. The dotted lines highlight the footprint of SLG (black dashed line), FLG (orange dashed line), hBN (blue dashed line), 1L-WS_2 (red dashed line). The green-shaded part corresponds to the active area$\sim$23μm^2. Cr/Au contacts the bottom SLG; FLG contacts the top 1L-WS_2. Schematic band diagram for (c) V=0V and (d) V>0V for pristine 1L-WS_2 LED and (e) V>0V for TFSI-treated 1L-WS_2 LED. Tuning the SLG E_F (gray dotted line) across the 1L-WS_2 valence band edge, E_V, allows h tunneling from SLG to 1L-WS_2, resulting in current onset and light emission via radiative recombination with e from the n-type 1L-WS_2. The blue circles represent e accumulated on 1L-WS_2 due to the MIS structure, while the red circles are h injected into 1L-WS_2 through the hBN barrier. The TFSI promotes a reduction of excess e in the 1L-WS_2

terized by Raman spectroscopy as discussed in Methods. After Raman characterization of all individual LMs on SiO_2/Si, the FLG/1L-WS_2/hBN/SLG LMH is assembled using dry-transfer as for Refs.[88, 89]. FLG is picked-up from SiO_2/Si using a polycarbonate (PC) membrane on a polydimethylsiloxane (PDMS) stamp (as mechanical support) at 40°C. We use 40°C because this is sufficient to increase the adhesion of the PC film[90], to pick all LMs from SiO_2/Si. Then, FLG is aligned to one edge of 1L-WS_2 on SiO_2/Si and brought into contact using xyz micromanipulators at 40°C, leaving the majority of 1L-WS_2 without FLG cover to be used as active area (AA). AA is the region from where light emission is expected, and it is the overlap area between 1L-WS_2 and SLG (green-shaded part in Fig.1b). Next, FLG/1L-WS_2 is aligned to a hBN flake deposited onto SiO_2/Si and brought into contact using xyz micromanipulators at 40°C. Finally, FLG/1L-WS_2/hBN is aligned to a SLG on SiO_2/Si and brought into contact using xyz micromanipulators at 180°C, whereby PC preferentially adheres to SiO_2[88], allowing PDMS to be peeled away, leaving PC/FLG/1L-WS_2/hBN/SLG on SiO_2/Si. PC is then dissolved in chloroform for$\sim$15mins at RT, leaving FLG/1L-WS_2/hBN/SLG LMH on SiO_2/Si[88, 89]. After LMH assembly, Cr/Au electrodes are fabricated by electron beam lithography (EBPG 5200, Raith GMBH), followed by metallization (1:50nm) and lift-off.

The tunnel junction based on a MIS structure consists of a LMH with 1L-WS_2 as the light emitter, FL-hBN (typically from 2 to 4nm) acting as tunnel barrier, and a SLG electrode to inject holes (h) into 1L-WS_2. We use FL-hBN<5nm so that a low (typically<5V) driving voltage is sufficient for charge injection to the 1L-WS_2[91, 92]. We employ FLG ($\sim$3-10nm) to contact 1L-WS_2, because FLG reduces the contact resistance[93], while Cr/Au electrodes give Ohmic contacts to SLG and FLG[93]. SLG could also be used to contact 1L-WS_2, however, as the optical contrast is higher in FLG than SLG[87, 94], using FLG makes it easier to align it to 1L-WS_2 during transfer. Since TFSI treatment requires direct exposure of 1L-TMDs[57], we place 1L-WS_2 on top of the stack to compare the device performance before and after treatment. We TFSI-treat 4 samples for EL and gated-PL measurements. These are immersed in a TFSI solution (0.2 mg/mL) in a closed vial for 10mins at 100°C[57–59], then removed, dried by a N_2 gun, and annealed on a hot plate at 100°C for 5mins[57–59]. Fig.1b is an image of the 1L-WS_2-LEDs. The FLG electrode is placed on the side of the SLG to avoid direct tunneling of carriers from SLG to FLG, hence keeping as AA the LMH region extended over SLG and 1L-WS_2, green-shaded in Fig.1b. If there is a FLG/SLG overlap, tunneling through FLG-SLG may be possible, not resulting in e-h recombination into 1L-WS_2, hence no EL[6, 25, 38].

Figs.1c,d sketch the band diagram of our LEDs for V=0V and V>0V, respectively. For V=0V (at thermodynamic equilibrium as indicated in Fig.1c), the Fermi level, E_F, is constant across the junction, and the net current (I) is zero[6, 21, 25, 28, 38]. For V>0V (positive potential on SLG), the SLG E_F is shifted below the 1L-WS_2 valence band energy E_V (Fig.1d), and h from SLG tunnel across the hBN barrier into 1L-WS_2, promoting EL emission by radiative recombination between the injected excess h and intrinsic e[21–24, 28, 35, 38]. The EL emission is expected to increase as a function of tunneling current because of the increasing h injected into 1L-WS_2 available for e-h recombination.

The LMs are characterized by Raman, PL, EL spectroscopy using a Horiba LabRam HR Evolution. The Raman spectra are collected using a 100x objective with numerical aperture (NA)=0.9, and a 514.5nm laser with a power$\sim$5μW to avoid damage or heating. The voltage bias dependent PL and EL are collected using a long working distance 50x objective (NA=0.45). For the PL spectra, we use a λ=532nm (2.33eV) continuous-wave laser in order to excite above the X^0 emission ($\sim$2eV)[9, 10]. The laser power is kept$\sim$80nW to avoid laser-induced thermal effects[2, 9–11]. The spot size A_{spot} for the PL measurements was calculated by A_{spot} =

Accepted Manuscript

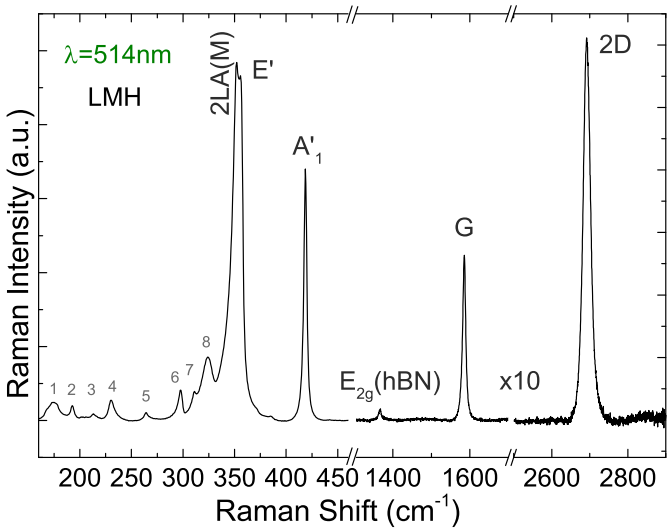

FIG. 2. 514.5nm Raman spectrum of 1L-WS_2/hBN/SLG LMH after device fabrication. The SLG and hBN Raman modes are labelled. The 1L-WS_2 modes are summarized in Table II. The 1300-2900cm^{-1} spectral window is multiplied by a factor 10 for better visualization

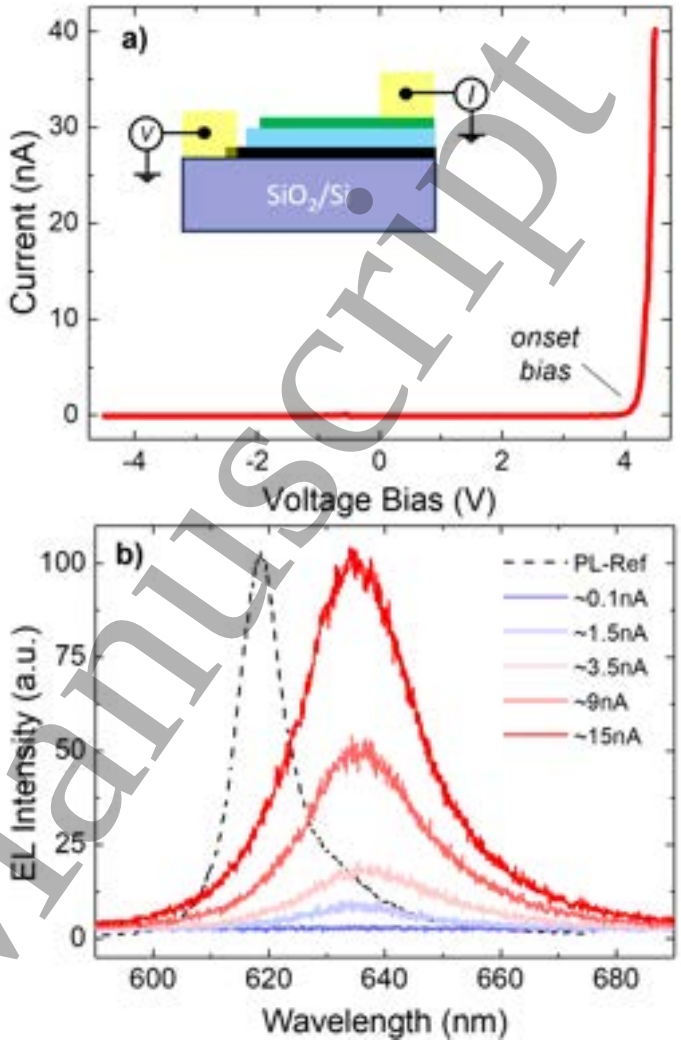

FIG. 3. a) I as a function of V for 1L-WS_2-LED. Inset: schematic of I-V data collection. Purple, SiO_2(300nm)/Si substrate; black, SLG; blue, hBN; green, 1L-WS_2; yellow, Cr/Au electrodes. The voltage V is applied while the current I is measured. b) EL spectra for different tunneling currents without TFSI treatment. The dashed black line is the PL spectrum for V=0, normalized to the maximum EL intensity

$\pi[1.22\lambda/2\mathrm{NA}]^2 \sim 1.6\mu\mathrm{m}^2$. The voltage ($V$) and current ($I$) between source (SLG) and drain (1L-WS_2) electrodes are set (V) and measured (I) by a Keithley 2400 (see Methods for details of electrical measurements).

Fig.2 plots the Raman spectrum of 1L-WS_2/hBN/SLG on Si/SiO_2 after device fabrication and before current-voltage (I-V) measurements. The Raman modes of each LM can be identified, Table II. For 1L-WS_2, Pos(A_1') and its full width af half maximum, FWHM(A_1'), change from$\sim$418.9$\pm$0.2cm^{-1}; 3.9$\pm$0.2cm^{-1}, before assembly, to$\sim$419.8$\pm$0.2cm^{-1}; 3.4$\pm$0.2cm^{-1}, after. All the changes in the other modes are close to our spectral resolution and errors, as for Ref.[95]. Pos(A_1') and FWHM(A_1') are sensitive to changes in n-doping[96, 97]. The mechanism responsible for this effect is an enhancement of electron-phonon (e-ph) coupling when e populate the valleys at K and Q simultaneously[97]. The energy of the K and Q valleys is modulated by the A_1' ph[97]. Since the K and Q energies are modulated out-of-phase, charge transfer between the two valleys occurs in presence of the A_1' ph[96, 97]. When the K and Q valleys are populated by e, these are transferred back and forward from one valley to the other[97, 98]. This increases the e-ph coupling of out-of-plane modes, such as A_1'[97]. The same process does not occur for p-doping[97]. The reason for this asymmetry between n- and p-doping is due to a much larger energy separation ($\sim$230meV[97]) between the VB Γ and K valleys than that ($\sim$100meV[97]) of the CB K and Q valleys. From the changes in Pos(A_1') and FWHM(A_1'), and by comparison with Ref.[97], we estimate a reduction in n-doping$\sim 5\times10^{12}$cm^{-2}.

For hBN in Fig.2, Pos(E_{2g})$\sim$1366.4$\pm$0.2cm^{-1} and FWHM(E_{2g})$\sim$9.2$\pm$0.2cm^{-1}. Although FWHM(E_{2g}) changes within the error, Pos(E_{2g}) downshifts$\sim$2.1cm^{-1} after assembly, suggesting a contribution from strain (see Methods for comparison between FL- and bulk-hBN Raman). Uniaxial strain lifts the degeneracy of the E_{2g} mode and results in the splitting in two subpeaks E_{2g}^+ and E_{2g}^-, with shift rates$\sim$-8.4 and -25.2cm^{-1}/%[99, 100]. For small levels of uniaxial strain (<0.5%) splitting cannot be observed and the shift rate is$\sim$-16.8cm^{-1}/%[99, 100]. For biaxial strain, splitting does not occur and E_{2g} shifts with rate$\sim$-39.1cm^{-1}/%[99]. Since we do not observe splitting, the E_{2g} shift can be attributed to uniaxial or biaxial tensile strain$\sim$0.13% or$\sim$0.06%, respectively.

For SLG in Fig.2, no D peak is observed

Accepted Manuscript

TABLE II. Pos and (FWHM) in cm^{-1} of WS_2 Raman peaks, before and after LMH assembly, and TFSI treatment

Peak	Bulk-WS_2 Assignment	Bulk-WS_2	1L-WS_2 Assignment	1L-WS_2-SiO_2	1L-WS_2-LMH	TFSI + 1L-WS_2-LMH
1	LA(M)	174.5 (11.1)	LA(M)	175.6 (14.5)	175.6 (14.6)	174.9 (14.4)
2	LA(K)	194.8 (3.3)	LA(K)	193.3 (4.5)	193.8 (3.3)	193.3 (4.7)
3	A_{1g}(K)-LA(K)	213.7 (4.2)	$A_1^{'}$(K)-LA(K)	214.5 (5.7)	214.5 (5.2)	213.5 (6.0)
4	A_{1g}(M)-LA(M)	232.8 (5.7)	$A_1^{'}$(M)-LA(M)	231.5 (6.7)	231.9 (7.1)	231.4 (5.9)
5	A_{1g}(M)-ZA(M)	266.8 (6.9)	$A_1^{'}$(M)-ZA(M)	265.3 (6.9)	265.9 (7.2)	265.4 (7.0)
6	$E^2_{2g}(\Gamma)$	297.6 (4.2)	$E^{''}(\Gamma)$	297.7 (2.8)	298.5 (3.1)	298.7 (2.6)
7	LA(M)+TA(M)	311.2(2.4)	LA(M)+TA(M)	311.2 (2.5)	311.8 (2.3)	311.2 (2.4)
8	E^2_{2g}(M)	324.6 (17.5)	$E^{''}$(M)	326.7 (25.5)	325.9 (24.7)	327.7 (25.7)
	2LA(M)	350.6 (8.3)	2LA(M)	352.4 (9.3)	352.7 (9.2)	352.7 (8.0)
	$E^1_{2g}(\Gamma)$	356.9 (1.5)	$E^{'}(\Gamma)$	357.2 (3.3)	357.4 (3.1)	357.2 (2.9)
	$A_{1g}(\Gamma)$	420.8 (2.1)	$A_1^{'}(\Gamma)$	418.9 (3.9)	419.8 (3.4)	419.9 (3.4)

after LMH assembly, indicating negligible defects[101–103]. In Fig.2 Pos(G)$\sim$1585.1$\pm$0.2cm^{-1}, FWHM(G)$\sim$9.0$\pm$0.2cm^{-1}, Pos(2D)$\sim$2692.3$\pm$0.2cm^{-1}, FWHM(2D)$\sim$20.9$\pm$0.2cm^{-1}, I(2D)/I(G)$\sim$2.4, and A(2D)/A(G)$\sim$5.6. These indicate that the SLG is p-doped, with E_F $\sim$150$\pm$50meV[102–104] by taking into account the average dielectric constant ($\sim$3.85) of the environment (ε_{SiO_2} $\sim$3.8[105] and ε_{hBN} $\sim$3.9[106]). E_F $\sim$150meV should correspond to Pos(G)$\sim$1584.1cm^{-1} for unstrained SLG[107]. However, Pos(G)$\sim$1585.1$\pm$0.2cm^{-1}, which implies a contribution from compressive uniaxial (biaxial) strain$\sim$0.04% ($\sim$0.01%). The strain level for SLG and hBN are different, most likely due to the fact that the SLG is directly exfoliated onto SiO_2/Si, while hBN is picked up and transferred by PDMS stamps, hence, this could induce a larger amount of strain on hBN.

Fig.3a plots the I-V characteristics. For V=0V the current is zero (Fig.1c). When V is applied, an electrical rectification (i.e. diode behavior) with negligible leakage current ($I<10^{-11}$A) for $V<0$ is seen. A tunneling onset, (i.e. exponential increase of I) is seen at $V_{ON}\sim$4.1V, Fig.3a. V_{ON} is related to the breakdown electric field (E_{bd}) across the junction, which depends on the voltage drop on the hBN tunnel barrier and hBN thickness (d) accordingly to $E_{bd}=(V_{bd}/d)\sim$0.7-1V/nm[91, 92], where V_{bd} is voltage breakdown $V_{bd}=qnd^2/(\varepsilon_0\varepsilon_{hBN})$, q is the e charge, n is total charge concentration, $\varepsilon_0=8.854\times10^{-12}$ F/m and ε_{hBN} $\sim$3.9[91, 92], so that V_{ON} can vary between different devices. When $V>V_{ON}$, h from SLG tunnel across the hBN barrier into 1L-WS_2, promoting EL emission by radiative recombination between the injected h and majority e in 1L-WS_2 (Fig.1c)[21–24, 35, 38]. The EL intensity$\sim$634nm ($\sim$1.956eV) increases with tunneling current, as in Fig.3b. The red-shifts (<2nm) in the EL emission in Fig.3b for larger I can be attributed to the E_F shift induced by the MIS structure[6, 31, 33]. FWHM(EL) also increases with I, attributed to the scattering of excitons with extra carriers[6, 109]. This shift and EL broadening is attributed to heating effects at the layered junction[28]. A red-shift$\sim$48meV is observed in EL emission$\sim$634nm ($\sim$1.956eV) with respect to the PL X^0 emission of the unbiased device (dashed black line, Fig.3b). Fig.3b shows a EL peak position close to X^- of unbiased PL (dashed black line, Fig.3b), implying a trionic EL emission, due to excess e in 1L-WS_2[28, 38]. In contrast, no light emission is observed for $V<0V$ and small positive ($0<V<V_{ON}$) bias, below the tunneling condition (V_{ON}<4.1V).

To further understand the EL emission origin, we perform EL and PL spectroscopy at the same V. Fig.4a plots PL spectra at different V. At V=0V, the PL peak is$\sim$619.2nm ($\sim$2.002eV), assigned to X^0[9, 78]. By increasing V (i.e. increasing e density in 1L-WS_2), a second peak appears at longer wavelengths ($\sim$630nm,$\sim$1.968eV), due to X^-[9–11, 108]. The dashed lines in Fig.4a describe the peak position evolution of X^0 and X^- emission for different V. For $V>$0V, the X^0 intensity gradually decreases and nearly vanishes, while X^- shifts to longer wavelengths, Fig.4a, reaching a similar position for both EL and PL emission (see Methods for further details). Fig.4a demonstrates that the gated-PL data show multipeak emissions at certain V (i.e. 0V$<V_{ON}$) due to injection of charge carriers from SLG to 1L-WS_2, allowing the recombination of both X^0 and X^-, whereas for n-doping ($V>>$0V), only X^- recombination takes place. This is expected for trionic emission, due to e-doping induced by V[9–12, 38, 108]. Similar effects were observed in 1L-MoS_2/SiO_2/Si[111], hBN/1L-WSe_2/hBN/SiO_2/Si[6], and hBN/1L-WS_2/hBN/SiO_2/Si[28]. Therefore, for similar tunneling current, EL agrees in energy and shape with the PL emission, further verifying the same origin for EL and PL, Fig.4b. This is confirmed by Fig.4c, where EL and PL peak positions are plotted for 4 devices, showing EL and PL emission at similar wavelengths. Thus, EL predominantly originates from X^-[6, 9, 10, 21, 38]. The variations in X^- for different

Accepted Manuscript

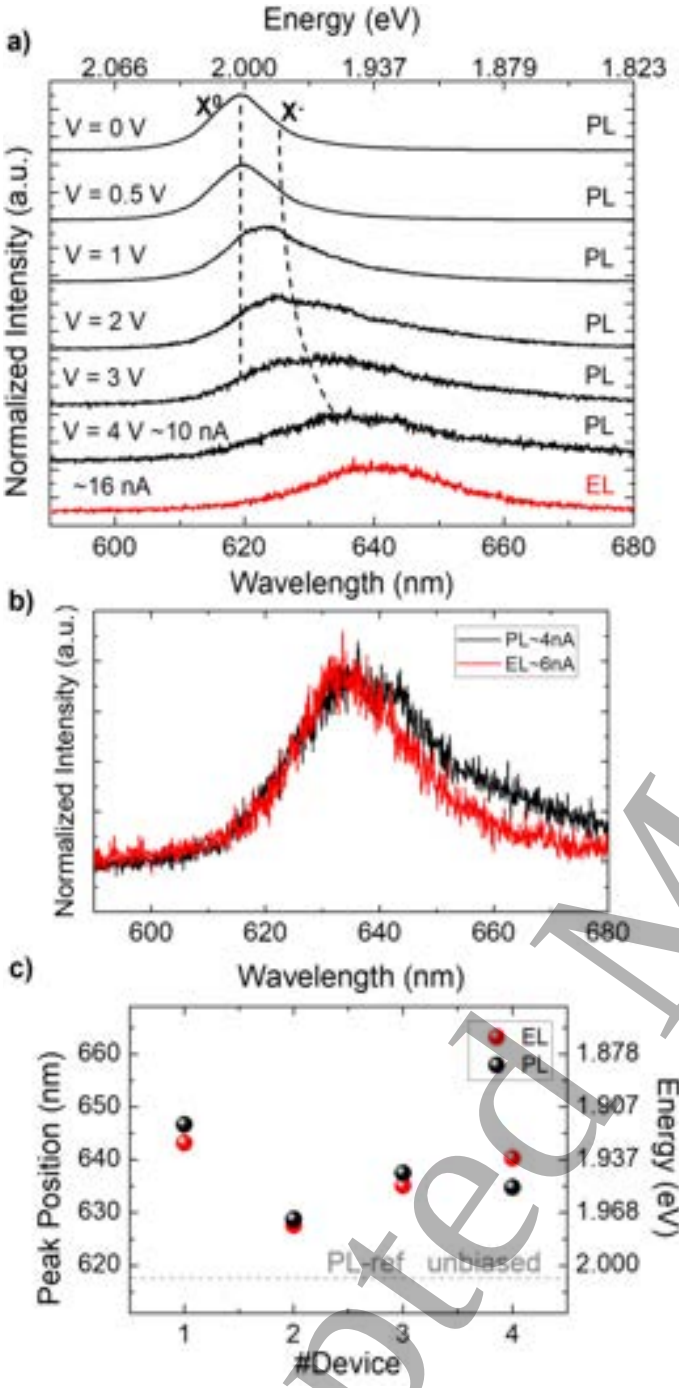

FIG. 4. a) Evolution of PL as a function of V. For comparison, an EL spectrum for I∼16nA is shown (red). The dashed lines are guides to the eye for the X^0 and X^- positions. In all PL measurements up to 3V, $I<10^{-11}$A. At 4V, $I\sim$10nA, indicating h tunneling through hBN into 1L-WS_2. b) Normalized gated-PL and EL spectra of a representative 1L-WS_2 LED near the threshold bias highlighting similarity of the emission spectra. c) EL and PL positions from 4 different devices. The dashed line plots the unbiased PL position of X^0 measured in Fig.3b. The emission values in (c) are derived by fitting with Lorentzians the PL and EL spectra at similar I level, considering the centre of the main emission peak (higher spectral weight). The error bars are within the size of the symbols

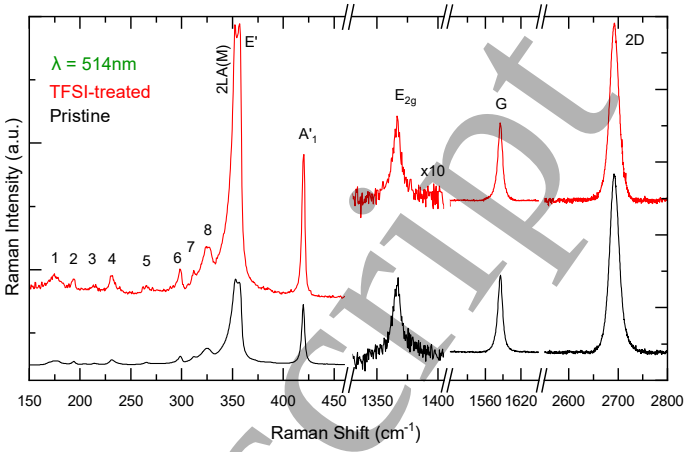

FIG. 5. 514.5nm Raman spectra of pristine (black line) and TFSI-treated (red line) 1L-WS_2/hBN/SLG. The SLG and hBN Raman modes are labelled, as well as the modes for 1L-WS_2, as for Table II. The 150-450cm^{-1} (1300-2800cm^{-1}) ranges are normalized to the Si (2D) peaks, respectively. The E_{2G} peak is multiplied by 10 for better visualization

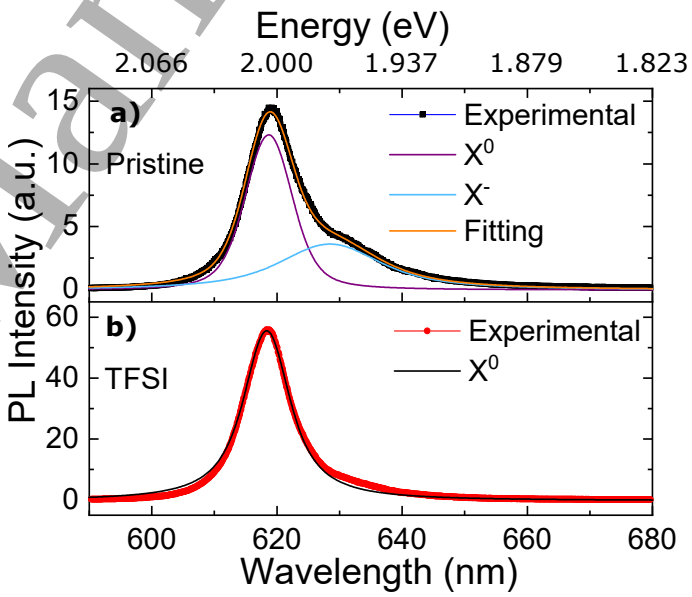

FIG. 6. Fitting of PL spectra for (a) pristine and (b) TFSI-treated 1L-WS_2 on SiO_2/Si, for 532nm excitation

LEDs are due to changes in charge carriers density across different samples. The charge density variation can be due to the number of vacancies in 1L-WS_2[41] and external impurities (PC residues and adsorbed water) after LED fabrication, which may vary from sample to sample.

We now consider the origin and consequences of excess e in 1L-WS_2 for EL emission induced by V. Besides the intrinsic charge carriers in 1L-WS_2 (typically n-type due to S vacancies[41]), there is also an electrostatically induced charge in 1L-WS_2 when $V>0$V. A SLG/hBN/1L-WS_2 tunneling junction acts as a MIS capacitor[6, 28, 38]. When $V>0$ is applied to SLG, inducing positive charges

Accepted Manuscript

in SLG, there is an opposite (negative) charge induced in 1L-WS_2[6, 28, 38], thus making the charge density on 1L-WS_2 larger than for V=0. When $V > V_{ON}$, h will be injected by tunneling into 1L-WS_2 (Fig.1d), hence, h will recombine with e. Consequently, the EL emission originates from X^- states. However, the radiative recombination efficiency (defined as the number of e-h pairs that recombine by emission of a photon divided by total number of e-h pairs) of X^- is lower than X^0 because of the small (∼30meV) binding energy of trions[42]. Thus, to gain higher η_{EL} one should favor X^0 EL emission by lowering the unbalanced free-carriers concentration in 1L-TMDs by either gate modulation[6, 12, 28, 31, 36, 38], physical[112, 113], or chemical doping[11, 25].

We thus treat 1L-WS_2 using TFSI to reduce doping and favor X^0 emission under bias and investigate the effects on EL emission and gated-PL. Fig.5 plots representative Raman spectra before (black) and after (red) TFSI treatment. By comparing the spectra before and after TFSI treatment, and the fits for 1L-WS_2 in Table II, we do not observe significant changes in peak position and FHWM. However, there is an overall intensity increase of the Raman peaks of∼50%, compared to the Si peak. This indicates a reduction of n-doping induced by TFSI treatment, because S vacancies in 1L-TMDs are commonly associated to n-type behaviour and the reduction of these defects will reflect in p-type doping fingerprint[57–59, 69]. Pos(A_1') is unaffected by TFSI treatment, which suggests that the reduction in the intrinsic 1L-WS_2 n-doping induced by TFSI is$<<10^{12}$cm^{-2}[97]. Although TFSI is able to p-dope SLG when it is in contact with the TFSI solution[114], Fig.5 shows negligible (within the errors[95]) changes in the SLG (e.g. before (after): Pos(G)∼1585.1 (1585.0)±0.2cm^{-1}, FWHM(G)∼9.0 (9.1)±0.2cm^{-1}, Pos(2D)∼2692.3 (2692.2)±0.2cm^{-1}, FWHM(2D)∼20.9 (20.8)±0.2cm^{-1}, I(2D)/I(G)∼2.4 (2.4), and A(2D)/A(G)∼5.6 (5.6)) and hBN (e.g. before (after): Pos(E_{2g})∼1366.4 (1366.5)±0.2cm^{-1} and FWHM(E_{2g})∼9.2 (9.1)±0.2cm^{-1}) Raman spectra after treatment, as both are protected by the top 1L-W_2.

Fig.6a plots a representative PL spectrum of 1L-WS_2 embedded in the LMH before TFSI treatment, and Fig.6b after. For the pristine case, there are two components, fitted by two Lorentzians∼618.7nm with FHWM∼8.4nm and∼629.1nm with FHWM∼18.1nm, which correspond to X^0[78, 80] and X^- emission, respectively[108, 110]. The observation of the X^- emission and a broader FWHM(X^-)>FWHM(X^0) is related to the n-type doping behavior of the 1L-WS_2[115], which favors the X^- recombination. For non-biased devices, the spectral weight (defined as the area of each peak) of the PL emission indicates a majority emission due to X^0. After treatment, the PL emission evolves to a main single peak∼618.1nm with FHWM∼8.7nm, accompanied by a∼4-fold increase in PL intensity. The PL

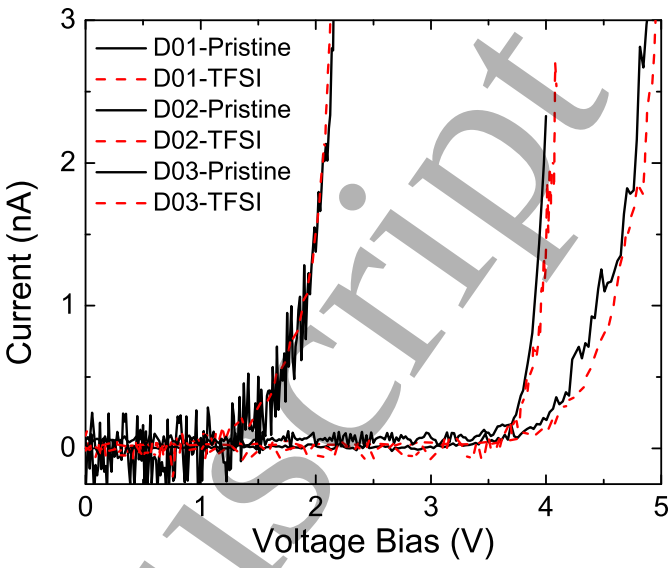

FIG. 7. I-V curves of 3 LEDs before (solid black lines) and after (dashed red lines) TFSI treatment.

intensity enhancement induced by the TFSI is consistent with that reported in Refs. [8, 49, 55, 57, 59, 60, 69, 70] The changes in spectral weight of X^0 and X^- emission and the FHWM after treatment can be assigned to a reduction in the e-density in 1L-WS_2[57–59], in agreement with our Raman analysis. Refs.[53–55, 57–68] reported that PL enhancement depends on sample quality (defects) and may vary 1 to 10 times. We observe a PL increase∼5±1-times, as for Refs.[53–55, 57–68].

Fig.7a plots typical I-V characteristics of 3 devices before (solid black lines) and after (dashed red lines) TFSI treatment. I is not affected by the treatment. V_{ON} is related to the breakdown electric field E_{bd} across the junction, which depends on the voltage drop on the hBN tunnel barrier and hBN thickness[91, 92]. Our LED-devices use 2 to 4nm hBN as tunnel barrier. Consequently, V_{ON} can vary between different devices. Our results on the same device demonstrate that TFSI treatment does not induce changes in the tunneling because the chemical treatment does not modify the MIS structure. Figs.9a,b show EL collected before and after TFSI, respectively, for different I. In both cases, EL is triggered for similar current levels (I<5nA), and the intensity increases linearly with I, Fig.9c. The EL intensity slope as a function of current density (I divided by AA) is affected by TFSI. For pristine-LEDs we get an average slope α ∼1.4±0.3, while after TFSI α ∼13.5±1.1, with 1 order of magnitude η_{EL} increase, Fig.9c. The red-shifts in the EL emission with I increase in pristine (<6nm) and TFSI treated LEDs (<5nm), Figs.9a,b, can be assigned to E_F shift induced by the MIS structure[6, 31, 33], or heating effects at the layered junction[28].

Next, we estimate the external quantum efficiency

Accepted Manuscript

(EQE) of our LEDs. This is defined as the ratio between the number of emitted photons (N_{ph}) and that of injected h per second (N_h)[116]:

$$EQE = \frac{N_{ph}}{N_h} = \frac{\sum_\lambda N_{ph-counts}}{N_h} \times \frac{A_{eff}}{\eta_{sys}}, \qquad (1)$$

where $\sum_\lambda N_{ph-counts}$ is the sum of the total photons collected by the spectrometer over the measured spectral range, $A_{eff} = AA/A_{spot}$, where A_{spot} is the microscope objective spot size $A_{spot} \sim 2.2\mu m^2$, with λ=618nm and NA=0.45), and $N_h = I \times t/q$, where t is the acquisition time, and q the e charge. The efficiency factor (defined as the ratio between the photons collected by the detector and the emitted photons by EL at the sample position) of our setup, including all optical components and spectrometer, is $\eta_{sys} \sim 0.0051$, see Methods.

From Eq.1 we get EQE$\sim$0.025%$\pm$0.021% and$\sim$0.195%$\pm$0.324% for pristine- and TFSI treated-LEDs, respectively, corresponding to a$\sim$8.7$\pm$1.5-fold increase, thus demonstrating that TFSI can boost EQE by almost one order of magnitude. EQE$\sim$0.2% is better than previously reported for 1L-WS_2-based EL ($\sim$0.1%) on a SiO_2/SiN_x microcavity[35], bulk organic (2,7-bis[9,9-di(4-methylphenyl)-fluoren-2-yl]-9,9-di(4-methylphenyl)fluorene) emissive layer ($\sim$0.1%)[117], and semiconducting (6,5) single-wall nanotubes ($\sim$0.1%)[118]. The WS_2-LED performance can be further improved if placed within a photonic cavity[25, 119–127].

To evaluate the cavity enhanced EQE, we extract the performance metrics from our reference measurements on SiO_2/Si and project them on simulation results for a cavity system. We first estimate the reference internal quantum efficiency $IQE_{ref} = EQE_{ref}/\eta_{(extr,ref)}$[116], where $\eta_{(extr,ref)}$ is the extraction efficiency on SiO_2/Si, defined as the number of photons emitted into free space over the total number of emitted photons[116]. Emitted photons not reaching free space include those absorbed and/or lost into the reference substrate. By 3d finite-difference time-domain method (FDTD) simulations[128, 129], of a $10\times10\mu m^2$ reference system with a single transverse electric (TE) (i.e. parallel to the surface) point dipole emitter on the surface at λ=624nm, we calculate $\eta_{(extr,ref)} \sim 14\%$, i.e., a significant ($\sim$86%) portion of the emitted light is absorbed and/or lost into the substrate. This yields for the TFSI-treated LED $IQE_{ref} \sim 1.43\%$. In turn, IQE_{ref} is related to the ratio of radiative to total recombination rates, i.e. $IQE_{ref} = \Gamma_{R,ref}/(\Gamma_{R,ref} + \Gamma_{NR})$[116, 130], where $\Gamma_{R,ref}$ and Γ_{NR} denote the radiative and non-radiative rates, respectively. For simplicity we assume $\Gamma_{NR} \equiv \Gamma_{NR,ref}$ independent of substrate, i.e., the non-radiative relaxation pathways are unaffected by the environment. Thus $\Gamma_{NR} = \Gamma_{R,ref}(IQE_{ref}^{-1} - 1)$. Inside a cavity, the radiative density of states increases, leading to a proportional increase in radiative rate due to the Purcell effect[130, 131]. Thus, $IQE_{cav} = \Gamma_{R,cav}/(\Gamma_{R,cav} + \Gamma_{NR})$, where $\Gamma_{R,cav} = \eta_P \Gamma_{R,ref}$ and η_P is the relative Purcell enhancement factor calculated by FDTD as the ratio of total light (free and lost) emitted by a point dipole in the cavity over the total light emitted on the reference substrate. Combining the above relations, we get $IQE_{cav}^{-1} = 1 + \eta_P^{-1}(IQE_{SiO_2/Si}^{-1} - 1)$. The external quantum efficiency becomes $EQE_{cav} = \eta_{extr,cav} IQE_{cav}$, with $\eta_{extr,cav}$ the extraction efficiency of the cavity evaluated by FDTD. The photonic cavity, shown in the top inset of Fig.8, is asymmetric to enable maximal unidirectional emission. Nb_2O_5/SiO_2 bilayers are used for the Bragg mirrors, with N_P Nb_2O_5/SiO_2 periods on top, a SiO_2 cavity in the middle, and an Ag back mirror. At λ=624nm the refractive indices are $n_{Nb_2O_5} = 2.325$[132],$n_{SiO_2} = 1.457$[133], $n_{Ag} = 0.0581 + i4.212$[134], $n_{SLG} = 2.787 + i1.443$[135, 136], $n_{hBN} = 2.12$[137], $n_{WS_2} = 5.38 + i0.382$[138]. The layer thicknesses are $d_{Nb_2O_5}$=67nm, d_{SiO_2}=107nm and d_{cav}=191nm, while IL-WS_2/hBN(3nm)/SLG is placed in the middle of the SiO_2 cavity layer. FDTD simulations predict the cavity enhanced EQE as a function N_P as for Fig.8. For N_P=1 the EQE gets a $\times$5.75 enhancement, reaching$\sim$1.15%, attributed to a Purcell enhancement of $\times$1.15 and a $\times$5 increase in extraction efficiency. Cavity effects also enhance the directionality of light, as shown in the bottom inset of Fig.8 for the SiO_2/Si reference structure as well as for the N_P=1 and N_P=2 cavity structures. To quantify the enhancement in the vertical direction (e.g. were we to use a narrow numerical aperture, NA=0.0125[127]), we also plot the normal emission enhancement through a 1d calculation in Fig.8. These are consistent with the angular plots of full 3d systems (lower inset of Fig.8) and predict an optimal cavity with N_P=3 and relative normal emissivity enhancement of $\times$16. Further enhancement mechanisms can also be considered, such as plasmonic cavities and/or antenna-coupling[139–145], as well as dielectric domes on top of the device to further boost extraction.

We now consider the EL emission features induced by TFSI treatment. By comparing EL before and after TFSI (Figs.9a,b), a blue-shift in EL is observed. In pristine-LEDs, the main EL emission can be fitted with a single Lorenztian at$\sim$641.8nm with FHWM$\sim$28.6nm, Fig.10a, whereas after treatment it can be fitted with two-Lorentzian$\sim$625.9nm with FHWM$\sim$28.6nm and $\sim$640.1nm with FHWM$\sim$29.2nm, Fig.10b. The observation of X^0 emission and similar FWHM(X^-) and Pos(X^-) after TFSI treatment suggests that there is a reduction in n-doping behavior, consistent with PL and Raman analysis. The fact that we observe X^- emission in EL after TFSI treatment indicates that 1L-WS_2 is still n-doped, which can be caused by e injection from the V bias in the MIS structure[6, 28, 33, 109]. Fig.10c plots the EL peak position before and after treatment in 4 devices. After treatment, the EL emission shifts to shorter wavelengths, where X^0 is expected[77, 78] (dashed line in

Accepted Manuscript

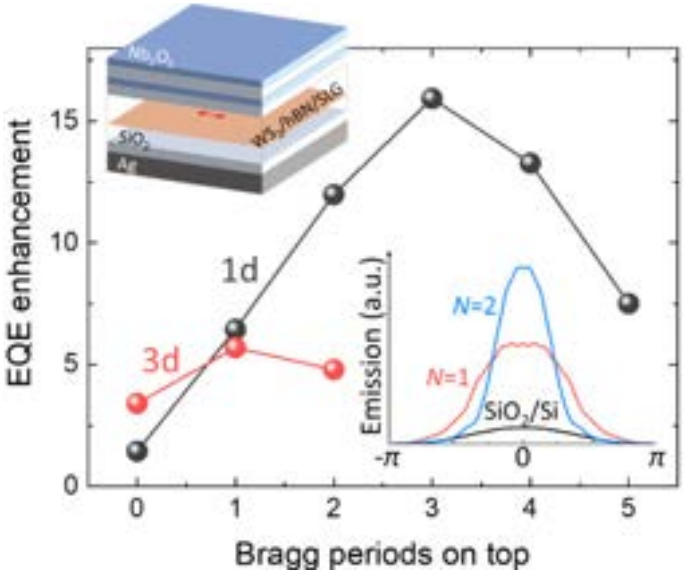

FIG. 8. TFSI-treated 1L-WS_2-LED enhanced EQE (3d calculation) in a cavity as a function of Bragg N_P periods (see top inset). Also plotted is the emissivity enhancement for vertical emission (1d calculation). The angular far-field intensity distribution for 3 device cases (3d calculations) is shown in the lower inset. All calculations are performed assuming $\lambda(EL) = 624nm$

Fig.10c). In non-biased S-based TMDs devices, this shift could be due to the depletion of excess e in n-doped 1L-WS_2 due to TFSI[57–62, 65–67]. Nevertheless, we cannot neglect the additional charge density induced by V on the MIS capacitor. E.g. the I-V characteristics in Fig.7 show that I and V_{ON} do not change before and after TFSI, suggesting the same tunneling condition is maintained across the 1L-WS_2/hBN/SLG junction. In both cases a comparable electric field (and charge) is developed across the junction for a given V. Fig.7 implies that, independent of TFSI treatment, the same amount of negative charge is electrostatically induced in 1L-WS_2 at $V>0$. However, taking into account the EL spectral shift towards X^0 emission upon bias, the expected depletion of excess e in 1L-WS_2 cannot explain the electrical behaviour of Figs.10b,c. Thus, the emission profile is not compatible with the I-V curves before and after TFSI in Fig.7, given that the electric field across the junction should be modified by the e density change in 1L-WS_2.

To get a better insight on the effects of TFSI on 1L-WS_2 based LEDs, Figs.10d,e plot normalized PL spectra as a function of V before and after TFSI. In the pristine case (Fig.10d), the PL map shows an evolution in emission spectra from∼620nm (∼2.000eV) to∼638nm (∼1.943eV), corresponding to a spectral shift from X^0 to X^- due to excess e in 1L-WS_2 induced by V. After TFSI treatment (Fig.10e), the PL exhibits only a minor shift from∼618nm (∼2.006eV) to∼622nm (∼1.993eV), implying that the induced e-charge in 1L-WS_2 does not con-

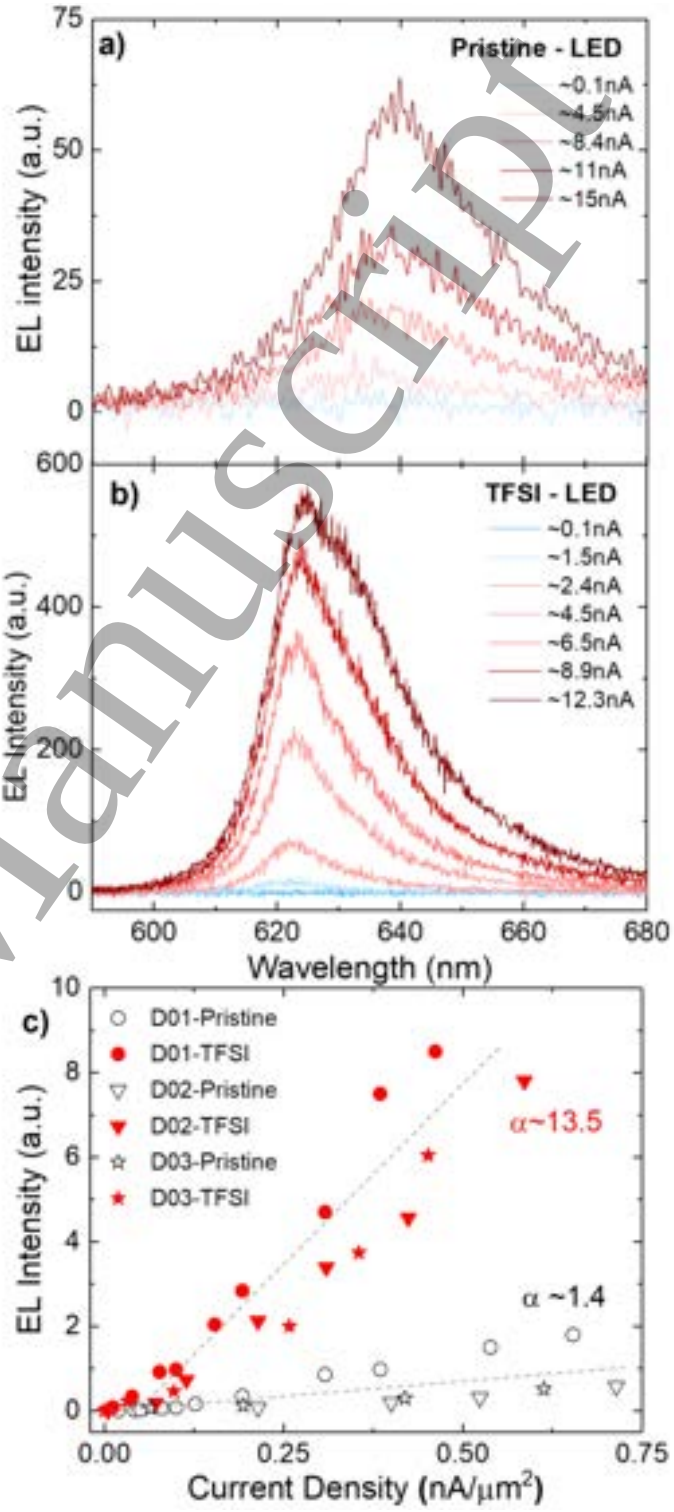

FIG. 9. EL spectra from (a) pristine and (b) TFSI-treated 1L-WS_2-LEDs for different tunneling currents. AA∼21μm^2. c) EL intensity as a function of tunneling current divided by AA for pristine (black) and TFSI-treated (red) 1L-WS_2-LEDs (3 devices). The dashed lines are a linear fit to the data. The emission values presented in (c) were taken by fitting with Lorentzians the EL spectra for every I, and the maximum intensity of the main EL peak was considered. The error bars for this fitting are within the size of the symbols presented

Accepted Manuscript

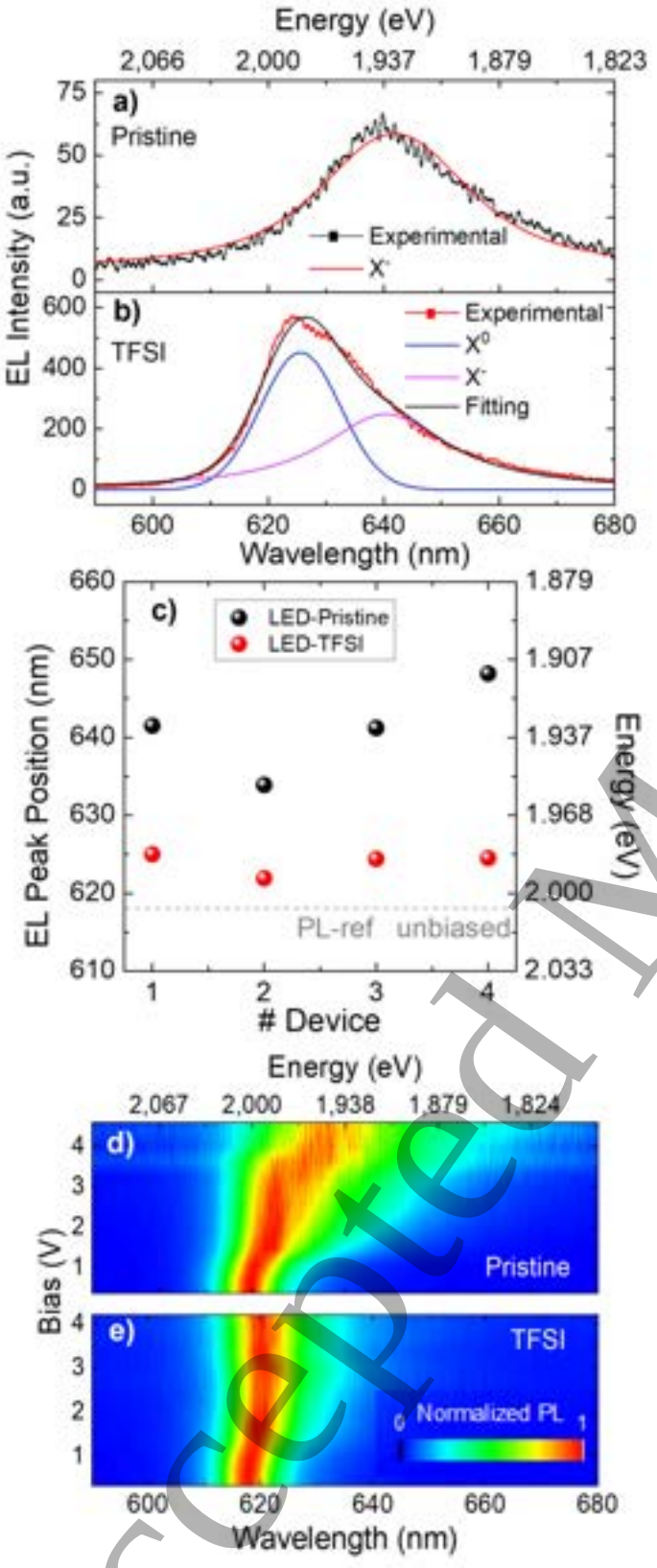

FIG. 10. EL spectra of (a) pristine and (b)TFSI-treated LEDs at similar tunneling current∼12nA, fitted with Lorentzians. c) Position of EL emission for different LEDs before (black) and after (red) TFSI. The values in (c) are fits with Lorentzians of EL spectra at similar I, considering the centre of the main emission peak (higher spectral weight). The error bars are within the size of the symbols. Color-plot of the gated-PL of (d) pristine and (e) TFSI-treated LED at similar laser excitation power and integration time

tribute to the X^- emission pathway. Therefore, similar to Figs.10a,b, PL also indicates that the emission after TFSI treatment predominantly originates from radiative recombination of X^0, independent of V. Refs.[57, 59, 61–64] claimed that TFSI treatment reduces the extent of n-type behavior in S-based 1L-TMDs due to S vacancies passivation, consistent with the suppression of X^- formation in Refs.[60, 65–68]. Ref.[8] reported that TFSI acts as a Lewis acid, i.e. it can accept an e pair from a donor[56], suppressing X^- formation. Whereas Refs.[53–55] claimed that TFSI may activate sub-gap states and reduce the n-type behavior in S-based TMDs, as well as reducing X^- formation. Our I-V, EL and gated-PL results suggest that TFSI treatment i) depletes the excess e in 1L-WS_2, acting as a Lewis acid[8] and ii) favours the radiative recombination of X^0 independent of bias, due to the activation of trapping states[53, 55] in 1L-WS_2 caused by the treatment. One would expect changes in the excitonic emission at such trapping states at RT, where the thermal energy can assist carrier de-trapping, and radiative recombination from excitons[67]. Therefore, the modification from non-radiative to radiative recombination by activation of trapping states could be further engineered to achieve more efficient optoelectronic devices.

CONCLUSIONS

We demonstrated a one order of magnitude enhancement in EL emission of 1L-WS_2-LEDs by performing TFSI treatment. EL predominantly originates from trions in pristine devices, while neutral excitons dominate in treated ones. The neutral excitonic emission is also restored in 1L-WS_2 gated-PL measurements. We attribute these changes to a reduction of n-doping of 1L-WS_2, as well as changes in the relaxation and recombination pathways within 1L-WS_2. This paves the way to more efficient 1L-TMDs-based LEDs, and sheds light into tunability of the excitonic emission of these devices.

METHODS

Raman characterization of LMH individual constituents

Raman spectroscopy allows us to monitor LMs at every step of device fabrication. This should always be performed on individual LMs before and after assembly in LMHs and devices. This is an essential step to ensure reproducibility of the results, but, unfortunately, this is often neglected in literature.

Ultralow-frequency (ULF) Raman spectra in the range∼10-50cm^{-1} probe shear (C), corresponding to layer motion parallel to the planes, and layer breathing modes (LBM), corresponding to the motion perpen-

Accepted Manuscript

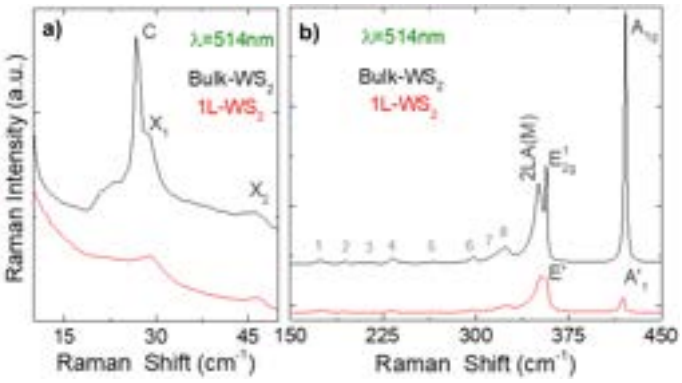

FIG. 11. (a) Low- and (b) high-frequency 514.5nm Raman spectra of 1L-WS_2 (red) and bulk-WS_2 (black) on Si/SiO_2, normalized to the Si peak, with labels as for Table II

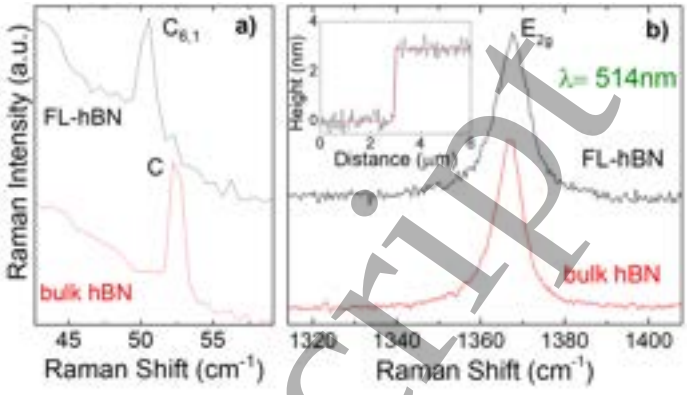

FIG. 12. (a) ULF and (b) HF 514.5nm Raman spectra of∼3nm hBN on Si/SiO_2 normalized to the Si peak. Inset: AFM height profile of∼3nm hBN on Si/SiO_2

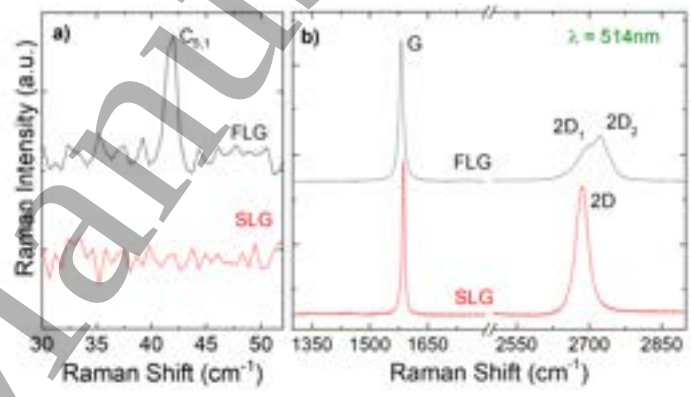

FIG. 13. (a) ULF and (b) HF 514.5nm Raman spectra of SLG and FLG on Si/SiO_2 normalized to the Si peak

dicular to them[102, 146–148]. $Pos(C)_N$ can determine the number of layers[146–149] $N=\pi(2\cos^{-1}[\frac{Pos(C)_N}{Pos(C)_\infty}])^{-1}$, with $Pos(C)_\infty$ the bulk Pos(C).

Fig.11 plots the Raman spectra of non-treated 1L-WS_2 and bulk-WS_2. In Fig.11a, the C mode and LBM are not observed for 1L-WS_2, as expected[146–148]. In bulk-WS_2, $Pos(C)\sim 26.9\pm0.14cm^{-1}$. The spectral resolution$\pm0.14cm^{-1}$ for the ULF region is obtained as for Ref.[95]. We observe two additional peaks$\sim28.7\pm0.14cm^{-1}$ and $46.4\pm0.14cm^{-1}$, respectively, in agreement with Refs.[150–152]. These do not depend on N[150, 151] and are seen because 514.5nm (∼2.41eV) is nearly resonant with the B exciton (∼2.4eV) of 1L-WS_2[153–157], and∼20meV above the bulk-WS_2 B exciton (∼2.38eV)[154, 155]. This gives rise to a resonant process[153–157], which occurs because the laser energy matches the electronic transition of the B exciton, revealing features associated with intervalley scattering mediated by acoustic ph[158–160]. A similar process also happens in 1L-MoS_2[150, 151] and other 1L-TMDs[158–160]. Although our ULF filters cut∼$5cm^{-1}$, the LBM is not detected in bulk-WS_2, as its frequency is expected to be$<10cm^{-1}$[148], because this resonant process with a 514.5nm laser reduces the signal to noise ratio in this spectral region[150].

The high-frequency (HF) Raman spectra of non-treated 1L-WS_2 and bulk-WS_2 (Fig.11b) show various peaks, Table II. The first order Raman modes, i.e. E', A_1' in 1L-WS_2[77–80] and E^1_{2g}, A_{1g} in bulk-WS_2[77–80]. E' ($E1_{2g}$) and A_1' (A_{1g}) correspond to in-plane and out-of-plane optical ph for 1L(bulk)-WS_2. Their nomenclature for 1L and bulk differs due to the different crystal symmetry[77–80]. In 1L-WS_2 we get $Pos(E')\sim356.8\pm0.2cm^{-1}$, $FWHM(E')\sim3.2\pm0.2cm^{-1}$, $Pos(A_1')\sim418.5\pm0.2cm^{-1}$, $FWHM(A_1')\sim4.3\pm0.2cm^{-1}$. In bulk-$WS_2$ we have $Pos(E^1_{2g})\sim356.8\pm0.2cm^{-1}$, $FWHM(E^1_{2g})\sim1.5\pm0.2cm^{-1}$, $Pos(A_1')\sim420.8\pm0.2cm^{-1}$, $FWHM(A_1')\sim2.1\pm0.2cm^{-1}$.

In 1L-WS_2 the difference in peaks' position [$Pos(E')$-$Pos(A_1')$] is$\sim61.7cm^{-1}$ while this is$\sim64.0cm^{-1}$ in bulk-WS_2, further corroborating the identification of 1L[77]. In the HF spectra of 1L- and bulk-WS_2 we also observe the 2LA(M) mode, involving two longitudinal acoustic (LA) ph close to the M point[77–79]. For 1L-WS_2 $Pos(2LA(M))\sim351.9\pm0.2cm^{-1}$ and $FWHM(2LA(M))\sim9.2\pm0.2cm^{-1}$, whereas for bulk-$WS_2$ $Pos(2LA(M))\sim350.6\pm0.2cm^{-1}$ and $FWHM(2LA(M))\sim8.3\pm0.2cm^{-1}$. The 2LA(M) mode originates from a second-order double resonant process[158–160], where momentum conservation is satisfied by two LA ph with opposite momenta around K- and M-points[159], therefore sensitive to differences in band structure between bulk and 1L-WS_2[77, 161].

$I(A_{1g})/I(E_{1g})\sim3.2$ in bulk-WS_2, with I is the peak height, is higher than $I(A_1')/I(E')\sim0.8$ in 1L-WS_2. $I(2LA)/I(E_{1g})\sim1$ in bulk-WS_2 is lower than $I(2LA(M))/I(E')\sim1.7$ in 1L-WS_2. This can be explained considering that the main first-order (E', A_1') and second-order (2LA(M)) Raman modes are enhanced for 2.41eV excitation, due to exciton-ph coupling effects involving

Accepted Manuscript

B exciton transitions[156, 162]. These depend on mode symmetry (i.e. differ between out-of-plane and in-plane modes) as well as N[158]. In bulk-WS_2, the out-of-plane A_{1g} is resonant with the B exciton, unlike E^1_{2g}[158]. The enhancement of A_{1g} decreases with decreasing N due to the dependence of the lifetime of the intermediate excitonic states on N[158]. The difference between I(2LA)/I($E^{'}_1$) in 1L-WS_2 and I(2LA)/I(E^1_{2g}) in bulk-WS_2 is due to a change in band structure from direct bandgap in 1L to indirect in bulk-WS_2[77–80], which changes the double resonance conditions[158–160].

The Raman spectrum of 1L-WS_2 also shows 8 peaks in the range 170-350cm^{-1} (Fig.10b and Table II). LA(M) and LA(K) correspond to one-ph processes originating from the LA branch at the M- and the K-points, respectively[77–80]. Since LA(M) and LA(K) and E^2_{2g}(M) are one-ph processes from the edge of the BZ (q≠0)[77–80], they should not be seen in the Raman spectra considering that, due to the Raman fundamental selection rule[163], one-ph processes are Raman active only for ph with q∼0, whereas for multi-ph scattering the sum of ph momenta needs to be∼0[158–161]. However these modes can be activated in presence of defects, as these can exchange momentum with ph, such that the sum of the momenta in the process is∼0[77–80]. A_{1g}(K)-LA(K), A_{1g}(M)-LA(M), A_{1g}(M)-ZA(M), LA(M)+TA(M) in bulk-WS_2 and $A^{'}$(K)-LA(K), $A^{'}_1$(M)-LA(M), $A^{'}_1$(M)-ZA(M), LA(M)+TA(M) in 1L-WS_2 are combinational modes, and Raman allowed[77–80]. E^2_{2g}(M) correspond to a one-ph process originating from the transverse optical (TO) branch at the M-point[77–80]. $E^2_{2g}(\Gamma)$ is a degenerate mode originating from the LO and TO branches at Γ[77–80].

Fig.12 plots the Raman spectra of a∼3nm hBN flake (black curves) and bulk-hBN (red curves). The latter has 2 Raman-active modes[164, 165], C and E_{2g}. In Fig.12a Pos(C)$_\infty$=52.3±0.14cm^{-1} with FWHM∼0.7±0.2cm^{-1} for bulk-hBN and Pos(C)$_N$=50.4±0.14cm^{-1} FWHM∼0.8±0.2cm^{-1} for the hBN flake. In bulk-hBN Pos(C)$_\infty$=$\frac{1}{\pi c}\sqrt{\frac{\alpha}{\mu}}$ =52.3cm^{-1}, with μ =6.9×10^{27}kgA^{-2} the mass of one layer per unit area, c the speed of light in cm s^{-1}, and α the spring constant associated to the coupling between the adjacent layers[95, 148]. From this, we get $\alpha = 16.9 \times 10^{18}$Nm^{-3}. From N=$\pi(2\cos^{-1}[\frac{Pos(C)_N}{Pos(C)_\infty}])^{-1}$, we get N=6±1 for the 3nm thick flake (measured with a Dimension Icon Bruker AFM in tapping mode) as shown in the inset of Fig.12b). In Fig.12b Pos(E_{2g})∼1368.5±0.2cm^{-1} and FWHM(E_{2g})∼9.1±0.2cm^{-1} for FL-hBN, and Pos(E_{2g})∼1367±0.2cm^{-1} with FWHM(E_{2g})∼7.6±0.2cm^{-1} for bulk-hBN. The peak broadening∼1.5cm^{-1} in FL-hBN can be attributed to strain variations within the laser spot, as thinner flakes conform more closely to the roughness of the underlying SiO_2[95]. This is consistent with the fact that thicker hBN have lower root mean square (RMS) roughness[88, 92, 95, 166], e.g. 300nm SiO_2 has RMS roughness∼1nm[92], 2-8nm hBN has RMS roughness∼0.2-0.6nm[95], while>10nm hBN thick presents RMS roughness∼0.1nm[88, 92].

The red curves in Figs.13a,b are the Raman spectra of SLG on SiO_2/Si before LMH assembly. Pos(G)=1586.9±0.2cm^{-1} with FWHM(G)=7.7±0.2cm^{-1}, Pos(2D)=2685.2±0.2cm^{-1} with FWHM(2D)∼29.3±0.2cm^{-1}, I(2D)/I(G)∼0.85, A(2D)/A(G)∼3.3. These indicate a p-doping[102–104] with E_F ∼ 200±50meV. No D peak is observed, thus negligible defects[101–103]. Pos(G) and Pos(2D) are affected by the presence strain[102, 103]. Biaxial strain can be differentiated from uniaxial from the absence of G-peak splitting with increasing ϵ[167, 168], however at low (≤0.5%) ϵ the splitting cannot be resolved[167, 168]. Thus, the presence (or coexistence) of biaxial strain cannot be ruled out. For uniaxial(biaxial) strain, Pos(G) shifts by ΔPos(G)/$\Delta\epsilon$ ≈23(60)cm^{-1}/%[167, 168]. Pos(G) also depends on doping[104, 107]. E_F ∼ 200±50meV should correspond to Pos(G)∼1584.3cm^{-1} for unstrained SLG[107]. However, in our experiment Pos(G)∼1586.9±0.2cm^{-1}, which implies a contribution from compressive uniaxial (biaxial) strain∼0.1% (∼0.04%). The black curves in Figs.12a,b show the Raman spectrum of the FLG electrode on SiO_2/Si. Pos(G)∼ 1581.2±0.2cm^{-1} with FWHM∼12±0.2cm^{-1}, Pos($2D_1$)∼ 2694.0±0.2cm^{-1} with FWHM∼48±0.2cm^{-1}, and Pos($2D_2$)∼ 2725±0.2cm^{-1} with FWHM∼33±0.2cm^{-1}. Pos(C)$_N$ ∼41.4±0.14cm^{-1}, corresponding to N=5.

Electrical characterization

Electrical characterization is performed at RT and in air, using two micrometric (xyz) positioners (Lambda EverBeing EB-050) with 10zmum W tips to provide signal and check the read-out. A Keithley 2400 sourcemeter is used as a DC source for the voltage potential V, with constant reading of the current I. The I-V curves are measured in a two-probe station, with one the probes touching the Cr/Au pad connecting the SLG, while the second connecting to the pad associated to 1L-WS_2. The 1L-WS_2 electrode is grounded to keep the electric field aligned from SLG towards 1L-WS_2, inducing e carries on 1L-WSe for V>0. For the I-V curves, the voltage sweep is 10mV/s and the data acquisition is interrupted as soon as I has exponential rise, to avoiding damage. The first measurement is the I-V curve, followed by EL, then, gated-PL spectra collection. For EL and gated-PL, the voltage is set manually to the desired V, then either EL or PL are acquired for 10 and 1s, respectively. A new V is then set by hand, followed by the next data acquisition. As soon as I reaches the values measured in the

Accepted Manuscript

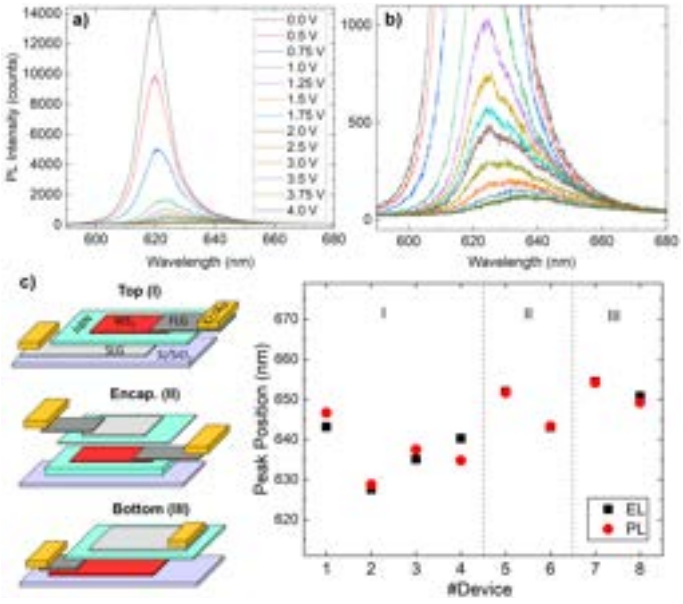

FIG. 14. a-b) Non-normalized gated-PL spectra for the data in Fig.4a. c) EL and gated-PL positions from 8 devices fabricated following different approaches: (I) Top: 1L-WS_2 on hBN and SLG. (II) Encap.: 1L-WS_2 encapsulated by 2 hBN (top and bottom), with SLG on the top-hBN. III) Bottom: 1L-WS_2 is sitting directly onto SiO_2/Si, capped with hBN and SLG. The emission values are taken by fitting with Lorentzians the PL and EL spectra at similar I, considering the center of the main emission peak (higher spectral weight). The error bars are within the size of the symbols

I-V curve, V is manually set back to zero. This guarantees that the devices can be measured at least 6 times (I-V, EL, and gated-PL before and after TFSI treatment) without damage.

Trionic PL and EL emission in 1L-WS_2 LEDs

Figs.14a-b show the gated-PL spectra with a continuous shift for larger V, with a$\sim$20nm shift, consistent with Ref.[28]. To further corroborate that both gated-PL and EL come from X^-, we fabricate 3 types of 1L-WS_2 based LEDs, Fig.14c: i) 1L-WS_2 on top of hBN and SLG layers; ii) 1L-WS_2 encapsulated by 2 hBN layers (top and bottom), and SLG on the top-hBN layer; iii) 1L-WS_2 sitting directly onto SiO_2/Si, capped with hBN and SLG. All devices are made following similar procedures. Electrical connection is done by applying V between SLG and 1L-WSV. The hBN tunnel barrier is 2-4nm thick. All devices are then checked by I-V measurements, gated-PL, and EL. Fig.14c demonstrates that all devices present a good match for EL and PL emission, in agreement with the X^- emission of Fig.4. We then TFSI treat 4 devices, those with 1L-WS_2 at the top of stack, allowing direct comparison before and after treatment.

Spectrometer efficiency

The η_{sys} of our spectrometer is derived as follows. We use a 50x objective (NA=0.45). Hence, the solid angle is θ=(1-cosθ)$\times 2\pi$, where θ=arcsin(NA/n), and n is the refractive index. Assuming n=1 we get θ=0.672. Thus, $M_{50x-eff}=\theta/(4\pi)\times 100\%\sim 5.4\%$. In our Horiba system, the optical path from M_{50x} to CCD includes 7 Mirrors (M_{eff} $\sim$83%), a slit (S_{eff} $\sim$90%), a grating (G_{eff} $\sim$60%) and a CCD detector (CCD_{eff} $\sim$85%). Therefore, the calculated overall collection+Horiba efficiency is: $M_{50x-eff}\times(M_{eff})^7\times S_{eff}\times G_{eff}\times CCD_{eff}$ $\sim$0.0067. To experimentally validate the calculation, we use a 0.5pW laser at 632.8nm and measure the counts at the CCD detector N_{counts}=149748. The photon energy at 632.8nm is $E_{ph}=(1.24/0.638)\times 1.6e^{-19}=3.13e^{-19}$J. The laser power is $P_{opt}=0.5e^{-12}$ J/s. As a result, if the system efficiency is 100% we expect to get $0.5e^{-12}/3.13e^{-19}$=1597444 counts. Therefore, the Horiba system efficiency is $Syst_{eff}$=149748/1597444=0.094. Considering $M_{50x-eff}$, we get an overall collection + Horiba efficiency $M_{50x-eff}\times Syst_{eff}=0.054\times 0.094=0.0051$, consistent with the theoretical estimation.

ACKNOWLEDGMENTS

We acknowledge funding from the EU Graphene and Quantum Flagships, EU grant Graph-X, ERC Grants Hetero2D and GSYNCOR and GIPT, EPSRC Grants EP/K01711X/1, EP/K017144/1, EP/N010345/1, EP/L016087/1, EP/V000055/1, EP/X015742/1

* Present address: Brazilian Nanotechnology National Laboratory, Brazilian Center for Research in Energy and Materials, São Paulo, Brazil
† Present Address: Micro- and Nanoelectronics Research Center, Technion, Haifa, Israel
‡ Present Address: Institute of Solid State Physics, Friedrich Schiller University Jena, MAx-Wien Platz 1 Jena 07743, Germany and Abbe Center of Photonics, Friedrich Schiller University Jena, Albert-Einstein-Straße 6 Jena 07745, Germany
§ acf26@eng.cam.ac.uk

[1] Schneider C, Glazov M M, Korn T, Hofling S and Urbaszek B, 2018 *Nat. Commun.* **9** 2695
[2] Wang G, Chernikov A, Glazov M M, Heinz T F, Marie X, Amand T and Urbaszek B, 2018 *Rev. Mod. Phys.* **90** 021001
[3] Mueller T and Malic E, 2018 *NPJ 2D Mater. Appl.* **2** 29
[4] Glazov M M, 2020 *J. Chem. Phys.* **153** 034703
[5] Barbone M, Montblanch A R, Kara D M, Palacios-Berraquero C, Cadore A R, de Fazio D, Pingault B,

Accepted Manuscript

Mostaani E, Li H, Chen B, et. al., 2018 *Nat. Commun.* **9** 3721
[6] Wang J, Lin F, Verzhbitshiy I, Watanabe K, Taniguchi T, Martin J and Eda G, 2019 *Nano Lett.* **19** 7470-7475
[7] Paur M, Molina-Mendoza A J, Bratschitsch R, Watanabe K, Taniguchi T and Mueller T, 2019 *Nat. Commun.* **10** 1709
[8] Lien D H, Uddin S Z, Yeh M, Amani M, Kim H and Anger III J W, Yablonovitch E and Javey A, 2019 *Science* **364** 468-471
[9] Zhu B, Chen X and Cui X, 2013 *Sci. Rep.* **5** 9218
[10] Shang J, Shen X, Cong C, Peimyoo N, Cao B, Eginligil M and Yu T, 2015 *ACS Nano* **9** 647-655
[11] Peimyoo N, Yang W, Shang J, Shen X, Wang Y and Yu T, 2014 *Nano Lett.* **8** 11320-11329
[12] Yang W, Shang J, Wang J, Shen X, Cao B, Peimyoo N, Zou C, Chen Y, Wang Y, Cong C, et. al., 2016 *Nano Lett.* **16** 1560-1567
[13] Ferrari A C, Bonaccorso F, Fal'ko V, Novoselov K S, Roche S, Bøggild P, Borini S, Koppens F H L , Palermo V, et. al., 2015 *Nanoscale* **7** 4598-4810
[14] Manzeli S, Ovchinnikov D, Pasquier D, Yazyev o V and Kis A, 2017 *Nat. Rev. Mater.* **2** 17033
[15] Bonaccorso F, Sun Z, Hasan T and Ferrari A C, 2010 *Nat. Photon.* **4** 611
[16] Koppens F H L, Mueller T, Avouris P, Ferrari A C, Vitiello M S and Polini M, 2014 *Nat. Nanotechnol.* **9** 780
[17] Romagnoli M, Sorianello V, Midrio M, Koppens F H L, Huyghebaert C, Neumaier D, Galli P, Templ W, D'Errico A and Ferrari A C, 2018 *Nat. Rev. Mater.* **3** 392–414
[18] Choi W, Choudhary N, Han G H, Park J, Akinwande D and Lee Y H, 2017 *Mater. Today* **20** 116
[19] Wang Z, Jingjing Q, Wang X, Zhang Z, Chen Y, Huang X and Huang W, 2018 *Chem. Soc. Rev.* **47** 6128-6174
[20] Zheng W, Jiang Y, Hu X, Li H, Zeng Z, Wang X and Pan A, 2018 *Adv. Optical Mater.* **6** 1800420
[21] Palacios-Berraquero C, Barbone M, Kara D M, Chen X, Goykhman I, Yoon D, Ott A K, Beitner J, Watanabe K, Taniguchi T, et. al., 2016 *Nat. Commun.* **7** 12978
[22] Jo S, Ubrig N, Berger H, Kuzmenko A B and Morpurgo A F, 2014 *Nano Lett.* **14** 2019-2025
[23] Withers F, Pozo-Zamudio O, Mishchenko A, Rooney A P, Gholinia A, Watanabe K, Taniguchi T, Haigh S J, Geim A K, Tartakovskii A I and Novoselov K S, 2015 *Nat. Mater.* **14** 301-306
[24] Withers F, Pozo-Zamudio O, Schwarz S, Dufferwiel S, Walker P M, Godde T, Rooney A P, Gholinia A, Woods C R, Blake P, Haigh S J, et. al., 2015 *Nano Lett.* **15** 8223-8228
[25] Liu C H, Clark G, Fryett T, Wu S, Zheng J, Hatami F, Xu X and Majmdar A, 2017 *Nano. Lett.* **17** 200-205
[26] Roman R J P, Auad Y, Grasso L, Alvarez F, Barcelos I D and Zagonel L F, 2020 *Nanoscale* **12**, 13460-13470
[27] Wang Q H, Kalantar-Zadeh K, Kis A, Coleman J N and Strano M S, 2012 *Nat. Nanotechnol.* **7** 699
[28] Kwak D, Paur M, Watanabe K, Taniguchi T and Mueller T, 2021 *Adv. Mater. Technol.* **7**, 2100915
[29] Zhu Y, Li Z, Zhang L, Wang B, Luo Z, Long J, Yang J, Fu L and Lu Y, 2018 *ACS Appl. Mater. Interfaces,* **10** 43291-43298
[30] Bie Y Q, Grosso G, Heuck M, Furchi M M, Cao Y, Zheng J, Bunandar D, Navarro-Moratalla E, Zhou L, Efetov D K, et. al., 2017 *Nat. Nanotechnol.* **12** 1124-1130
[31] Sundaram R S, Engel M, Lombardo A, Krupke R, Ferrari A C, Avouris P and Steiner M, 2013 *Nano Lett.* **13** 1416-1421
[32] Sheng Y, Chen T, Lu Y, Chang R J, Sinha S and Warner J H, 2019 *ACS Nano* **13** 4530-4537
[33] Andrzejewski D, Myja H, Heuken M, Grundmann A, Kalisch H, Vescan A, Kümmell T and Bacher G, 2019 *ACS Photonics* **6** 1832-1839
[34] Andrzejewski D, Hopmann E, John M, Kummell T and Bacher G, 2019 *Nanoscale* **11** 8372
[35] Gu J, Chakraborty B, Khatoniar M and Menon V M, 2019 *Nat. Nanotechnol.* **14** 1024-1028
[36] Ross J S, Klement P, Jones A M, Ghimire N J, Yan J, Mandrus D G, Taniguchi T, Watanabe K, Kitamura K, Yao W, et. al., 2014 *Nat. Nanotechnol.* **9** 268-272
[37] Baugher B W H, Churchill H O H, Yang Y and Jarillo-Herrero P, 2014 *Nat. Nanotechnol.* **9** 262-267
[38] Wang S, Wang J, Zhao W, Giustiniano F, Chu L, Verzhbitskiy I, Yong J S and Eda G, 2017 *Nano Lett.* **17** 5156-5162
[39] Yuan L and Huang L, 2015 *Nanoscale* **7** 7402-7408
[40] Wang H, Zhang C and Rana F, 2015 *Nano Lett.***15** 339–345
[41] Zhang Y J, Oka T, Suzuki R, Ye J T and Iwasa Y, 2014 *Science* **344** 725-728
[42] Jones A M, Yu H, Schaibley J R, Yan J, Mandrus D G, Taniguchi T, Watanabe K, Dery H, Yao W and Xu X, 2016 *Nature Phys.* **12** 323–327
[43] Lundt N, Cherotchenko E, Iff O, Fan X, Shen Y, Bigenwald P, Kavokin A V, Höfling S and Schneider C, 2018 *Appl. Phys. Lett.* **112** 031107
[44] Haug H and Koch S W, *Quantum theory of he optical and electronic properties of semiconductors* (World Scientific, Singapore, 2009).
[45] Klingshirn C, *Semiconductor Optics*, 3rd edition (Springer, Berlin, 2007).
[46] Kiriya D and Lien D-H, 2022 *Nano Ex.* **3** 034002
[47] Yao H, Liu L, Wang Z, Li H, Chen L, Pam M E, Chen W, Yang H Y, Zhang W and Shi Y, 2018 *Nanoscale* **10** 6105-6112
[48] Mouri S, Miyauchi Y and Matsuda K, 2013 *Nano Lett.* **13** 5944-5948
[49] Li Z, Bretscher H, Zhang Y, Delport G, Xiao J, Lee A, Stranks S D and Rao A 2021 *Nat. Commun.* **12** 6044
[50] Su W, Dou H, Li J, Huo W, Dai N and Yang L, 2015 *RSC Adv.* **5** 82924-92929
[51] Park J H, Sanne A, Guo Y, Amani M, Zhang K, Movva H C P, Robinson J A, Javey A, Robertson J, Banerjee S K, et al., 2017 Sci. Adv. **3** e1701661
[52] Kiriya D, Hijikata Y, Pirillo J, Kitaura R, Murai A, Ashida A, Yoshimura T and Funjimura N, 2018 *Langmuir* **34** 10243-10249
[53] Bretscher H M, Li Z, Xiao J, Qiu D Y, Refaely-Abramson S, Alexander-Webber J, Tanoh A O A, Fan Y, Delport G and Williams C, 2021 et. al., *ACS Nano* **15** 8780-8789
[54] Tanoh A O A, Alexander-Webber J, Fan Y, Gauriot N, Xiao J, Pandya R, Li Z, Hofmann S and Rao A, 2021 *Nanoscale Adv.* **3** 4216-4225
[55] Tanoh A P A, Alexander-Webber J, Xiao J, Delport G, Willians C A, Bretscher H, Gauriot N, Allardice J, Padya R, Fan Y, et. al., 2019 *Nano Lett.* **19** 6299-6307

Accepted Manuscript

[56] Himmel D, Goll S K, Leito I and Krossing I, 2010 *Angew. Chem. Int. Ed.* **49** 6885–6888
[57] Amani M, Lien D H, Kiriya D, Xiao J, Azcati A, Noh J, Madhvapathy S R, Addou R, KC S, Dubey M, et. al., 2015 *Science* **350** 1065-1068
[58] Amani M, Burke R A, Ji X, ZhaoP, Lien D H, Taheri P, Ahn G H, Kirya D, Ager III J W, Yablonovitch E, et. al., 2016 *ACS Nano* **10** 6535-6541
[59] Amani M, Taheri P, Addou R, Ahn G H, Kirya D, Lien D H, Ager III J W, Wallace R M and Javey A, 2016 *Nano Lett.* **16** 2786-2791
[60] Kim H, Liem D H, Amani M, Ager III J W and Javey A, 2017 *ACS Nano* **11** 5179-5185
[61] Molas M R, Golasa J, Bala L, Nogajewski K, Bartos M, Potemski M and Babinski A, 2019 *Sci. Rep.* **9**, 1989
[62] Roy S, Choi W, Jeon S, Kim D H, Kim H, Yun S J, Lee Y, Lee J, Kim Y M and Kim J, 2018 *Nano Lett.* **18** 4523-4530
[63] Alharbi A, Zah P and Shahrjerdi D, 2017 *Appl. Phys. Lett.* **110** 033503
[64] Cadiz F, Tricard S, Gay M, Lagarde D, Wang G, Robert C, Renucci P, Urbaszek B and Marie X, 2016 *Appl. Phys. Lett.* **108** 251106
[65] Zhang K, Borys N J, Bersch B M, Bhimanapati G R, Xu K, Wang B, Wang K, Labella M, Willians T A, Haque M A, et. al., 2017 *Sci. Rep.* **7** 16938
[66] Lin P, Zhu L, Li D and Wang Z L, 2019 *J. Mater. Chem. C* **7** 14731
[67] Goodman A J, Willard A P and Tisdale W A, 2017 *Phys. Rev. B* **96** 121404(R)
[68] Lu H, Kummel A and Robertson J, 2018 *APL Mater.* **6** 966104
[69] Dhakal K P, Roy S, Yun S J, Ghimire G, Seo C and Kim J, 2017 *J. Mater. Chem. C* **5** 6820
[70] Pain S L, Grant N E and Murphy J D, 2022 *ACS Nano* **16** 1260-1270
[71] Barbosa A N, Mendoza C A D, Lei Y, Girola M, Terrones M, Mariotto G and Junior F L F, 2022 *Surf. Interfaces* **33** 102220
[72] Han C, Wang Y, Zhou W, Liang M and Ye J, 2021 *Sci. Rep.* **11** 10080
[73] Qin C-B, Liang X-L, Han S-P, Zhang G-F, Chen R-Y, Hu J-Y, Xia L-T and Jia S-T, 2021 *Front. Phys.* **16** 12501
[74] Cheng F, Johnson A D, Tasi Y, Su P-H, Hu S, Ekerdt J G and Shih C-K, 2017 *ACS Photonics* **4** 1421-1430
[75] Kern JH, Trügler A, Niehues I, Ewering J, Schmidt R, Schneider R, Najmaei S, George A, Zhang J, Lou J, Hohenester U, de Vasconcellos S M and Bratschitsch R, 2015 *ACS Photonics* **2** 1260-1265
[76] Lien D-H, Amani M, Desai S B, Ahn G H, Han K, He J-H, Ager III J W, Wu M C and Javey A, 2018 *Nat. Commun.* **9** 1229
[77] Berkdemir A, Gutierrez H R, Botello-Mendez A R, Perea-Lopez N, Elias A L, Chia C H, Wang B, Crespi V H, Lopez-Urias F, Charlier J C, et. al., 2013 *Sci. Rep.* **3** 1755
[78] Gutierrez H R, Perea-Lopez N, Elias A L, Berkdemir A, Wang B, Lv R, Lopez-Urias F, Crespi V H, Terrones H and Terrones M, 2013 *Nano Lett.* **13** 3447-3453
[79] Molina-Sanchez A and Wirtz L, 2011 *Phys. Rev. B* **84** 155413
[80] Zhao W, Ghorannevis Z, Amara K K, Pang J R, Toh M, Zhang X, Kloc C, Tan P H and Eda G, 2013 *Nanoscale* **5** 9677-9683
[81] Nagao M 2017 *Condens. Matter* **2** 32
[82] Suchkov A B, Rumyantseva G V, Demachev A R and Zhukova N V, 1971 *Sov. Powder Metall. Met. Ceram.* **10** 941-942
[83] Montblanch A R P, Kara D M, Paradisanos I, Purser C M, Feuer M S G, Alexeev E M, Stefan L, Qin Y, Blei M, Wang G, et. al., 2021 *Commun. Phys.* **4** 119
[84] Edelberg D, Rhodes D, Kerelsky A, Kim B, Wang J, Zangiabadi A, Kim C, Abhinandan A, Ardelean J, Scully M, et. al., 2019 *Nano Lett.* **19** 4371-4379
[85] Watanabe K, Taniguchi T and Kanda H, 2004 *Nat. Mater.* **3** 404-409
[86] Novoselov K S, Jiang D, Schedin F, Booth T J, Khotkevich V V, Morozov S V and Geim A K, 2005 *Proc. Natl. Acad. Sci. U.S.A.* **102** 10451–10453
[87] Casiraghi C, Hartschuh A, Lidorikis E, Qian H, Harutyunyan H, Gokus T, Novoselov K S and Ferrari A C, 2007 *Nano Lett.* **9** 2711-2717
[88] Purdie D G, Pugno N M, Taniguchi T, Watanabe K, Ferrari A C and Lombardo A, 2018 *Nat. Commun.* **9** 5387
[89] Viti L, Cadore A R, Yang X, Vorobiev A, Muench J E, Watanabe K, Taniguchi T, Stake J, Ferrari A C and Vitiello M S, 2021 *Nanophotonics* **10** 89-98
[90] Pizzocchero F, Gammelgaard L, Jessen B S, Caridad J M, Wang L, Hone J, Boggild P and Booth T J, 2016 *Nat. Commun.* **7** 11894
[91] Hattori Y, Taniguchi T, Watanabe K and Nagashio K, 2015 *ACS Nano* **9** 916-921
[92] Mania E, Alencar A B, Cadore A R, Carvalho B R, Watanabe K, Taniguchi T, Neves B R A, Chacham H and Campos L C, 2017 *2D Mater.* **4** 031008
[93] Guimaraes M H D, Gao H, Han Y, Kang K, Xie S, Kim C J, Muller D A, Ralph DC and Park J, 2016 *ACS Nano* **10** 6392–6399
[94] Nair R R, Blake P, Grigorenko A N, Novoselov K S, Booth T J, Stauber T, Peres N M R and Geim A K, 2008 *Science* **320** 1308
[95] Chiodini S, Kerfoot J, Venturi G, Mignuzzi S, Alexeev E M, Rosa B T, Tongay S, Taniguchi T, Watanabe K, Ferrari A C, et. al., 2022 *ACS Nano* **16** 7589-7604
[96] Chakraborty B, Bera A, Muthu D V S, Bhowmick S, Waghmare U V and Sood A K, 2012 *Phys. Rev. B* **85** 161403(R)
[97] Sohier T, Ponomarev E, Gibertini M, Berger H, Marzari N, Ubrig N and Morpurgo A F, 2019 *Phys. Rev. X* **9** 031019
[98] Paradisanos I, Wang G, Alxeev E M, Cadore A R, Marie X, Ferrari A C, Glazov M M and Urbaszek B, 2021 *Nat. Commun.* **12** 538
[99] Androulidakis C, Koukaras E N, Poss M, Papagelis K, Galiotis C and Tawfick S, 2018 *Phys. Rev. B* **97** 241414(R)
[100] Cai Q, Scullion D, Falin A, Watanabe K, Taniguchi T, Chen Y, Santos E J G and Li L H, 2017 *Nanoscale* **9** 3059
[101] Cançado L G, Jorio A, Ferreira E H M, Stavale F, Achete C A, Capaz R B, Moutinho M V O, Lombardo A, Kulmala T S and Ferrari A C, 2011 *Nano Lett.* **11** 3190-3196
[102] Ferrari A C and Basko D M, 2013 *Nat. Nanotechnol.* **8** 235-256
[103] A.C. Ferrari, 2007 Solid State Commun. **143** 47-57

Accepted Manuscript

[104] Basko D M, Piscanec S and Ferrari A C, 2009 *Phys. Rev. B* **80** 1-10
[105] Kingon A I, Maria J-P and Streiffer J-P, 2000 *Nature* **406** 1032–1038
[106] Laturia A, van der Put M L and Vandenberghe W G, 2018 *NPJ 2D Mater. Appl.* **2** 1–7
[107] Das A, Pisana S, Chakraborty B, Piscanec S, Saha S K, Waghmare U V, Novoselov K S, Krishnamurthy H R, Geim A K, Ferrari A C and Sood A K, 2008 *Nature* Nanotech. **3** 210-215
[108] Paradisanos I, Germanis S, Pelekanos N T, Fotakis C, Kymakis E, Kioseoglou G and Stratakis E, 2017 *Appl. Phys. Lett,* **110** 193102
[109] Chernikov A, van der Zande A M, Hill H M, Rigosi A F, Velauthapillai A, Hone J and Heinz T F, 2015 *Phys. Rev. Lett,* **115** 126802
[110] Prando G A, Severijnen M E, Barcelos I D, Zeitler U, Christianen P C M, Withers F and Gobato Y G, 2021 *Phys. Rev. Applied* **16** 064055
[111] Mak K F, He K, Lee C, Lee G H, Hone J, Heinz T F and Shan J, 2013 *Nature Mater.* **12** 207-211
[112] Wang Y, Slassi A, Stoeckel M A, Bertolazzi S, Cornil J, Beljonne D and Samori P, 2019 *J. Phys. Chem. Lett.* **10** 540–547
[113] Tongay S, Zhou J, Ataca C, Liu J, Kang J S, Matthews T S, You L, Li J, Grossman J C and Wu J, 2013 *Nano Lett.* **13** 2831-2836
[114] Heo J H, Lee D S, Zhang F, Xiao C, Heo S J, Lee H J, Zhu K and Im S H, 2021 *Sol RRL.* **1** 2100733
[115] Cadiz F, Courtade E, Robert C, Wang G, Shen Y, Cai H, Taniguchi T, Watanabe K, Carrere H, Lagarde D, et. al., 2017 *Phys. Rev. X* **7**, 021026
[116] Schubert E F, *Light-Emitting Diodes*, 2nd Edition (Rensselaer Polytechnic Institute, New York, 2006).
[117] Gubbin CR, Maier SA, and Kéna-Cohen S, 2014 *Appl. Phys. Lett.* **104**, 233302
[118] Graf A, Held M, Zakharko Y, Tropf L, Gather MC, and Zaumseil J, 2017 *Nat. Mater.* **16**, 911-917
[119] Brotons-Gisbert M, Martínez-Pastor JP, Ballesteros GC, Gerardot BD, Sánchez-Royo JF. 2018 *Nanophotonics* **7**, 253–67.
[120] Dufferwiel S, Schwarz S, Withers F, Trichet AAP, Li F, Sich M, , Del Pozo-Zamudio O, Clark C, Nalitov A, Solnyshkov DD, et. al., 2015 *Nat Commun* **6**, 8579
[121] Galfsky T, Sun Z, Considine CR, Chou CT, Ko WC, Lee YH, Narimanov EE, and Menon VM, 2016 *Nano Lett* **16**, 4940–4945.
[122] Gan X, Gao Y, Fai Mak K, Yao X, Shiue RJ, van der Zande A, Trusheim ME, Hatami F, Heinz TF, Hone J, et. al., 2013 *Appl Phys Lett* **103**,181119.
[123] Javerzac-Galy C, Kumar A, Schilling RD, Piro N, Khorasani S, Barbone M, Goykhman I, Khurgin JB, Ferrari AC, and Kippenberg TJ, 2018 *Nano Lett***18**, 3138–3146.
[124] Liu X, Galfsky T, Sun Z, Xia F, Lin E chen, Lee YH, Kéna-Cohen S, and Menon VM,2015 *Nat Photonics* **9**, 30–34.
[125] Noori YJ, Cao Y, Roberts J, Woodhead C, Bernardo-Gavito R, Tovee P, and Young RJ, 2016 *ACS Photonics* **3**, 2515–2520.
[126] Lau EK, Lakhani A, Tucker RS, and Wu MC. 2009 *Opt Express* **17**, 7790
[127] Zamudio O D-P, Genco A, Schwarz S, Withers F, Walker P M, Godde T, Schofield R C, Rooney A P, Prestat E, Watanabe K, et. al., 2020 *2D Mater.* **1** 1-10
[128] Taflove A, *Computational Electrodynamics: The Finite-Difference Time- Domain Method*, Artech House, Norwood, MA, 1995
[129] Lumerical Inc. https://www.lumerical.com
[130] Pelton M, 2015 *Nat Photonics* **9**, 427
[131] Purcell EM, 1946 *Phys Rev* **69**, 681
[132] Horcholle B, Labbé C, Portier X, Marie P, Frilay C, Yuan W, Jadwisienczak W, Ingram D, Grygiel C, and Cardin J, 2022 *Appl Surf Sci* **597**, 153711
[133] Malitson IH, *J Opt Soc Am* **55**, 1205-1208
[134] Johnson PB and Christy R, 1972 *Phys Rev B* **6**, 4370
[135] Kravets VG, Grigorenko AN, Nair RR, Blake P, Anissimova S, Novoselov KS, and Geim AK, 2010 *Phys Rev B* **81**, 155413
[136] Echtermeyer TJ, Milana S, Sassi U, Eiden A, Wu M, Lidorikis E, and Ferrari AC, *Nano Lett* **16**, 8-20
[137] Lee SY, Jeong TY, Jung S, and Yee KJ, 2018 *Phys Status Solidi B* **256**, 1800417
[138] Hsu C, Frisenda R, Schmidt R, Arora A, De Vasconcellos SM, Bratschitsch R, van der Zant HSJ, and Castellanos-Gomez A, 2019 *Adv Opt Mater* **7**, 1900239.
[139] Ma L, Yu P, Wang W, Kuo H, Govorov AO, Sun S, and Zhiming W, 2021 *Laser Photonics Rev* **15**, 2000367
[140] Chen H, Yang J, Rusak E, Straubel J, Guo R, Myint YW, Pei J, Decker M, Staude I, Rockstuhl C, et. al., 2016 *Sci Rep* **29**, 22296
[141] Kinkhabwala A, Yu Z, Fan S, Avlasevich Y, Müllen K, and Moerner WE. 209 *Nat Photonics* **3**, 654–657
[142] Eggleston MS, Desai SB, Messer K, Fortuna SA, Madhvapathy S, Xiao J, Zhang X, Yablonovitch E, Javey A, and Wu MC, 2018 *ACS Photonics* **5**,2701–2705
[143] Eggleston MS, Messer K, Zhang L, Yablonovitch E, and Wu MC. 2015 *Proc Natl Acad Sci* **112**,1704–1709
[144] Sortino L, Zotev PG, Mignuzzi S, Cambiasso J, Schmidt D, Genco A, Abmann M, Bayer M, Maier SA, Sapienza R, et. al., 2019 *Nat Commun* **10**, 5119
[145] Bitton O and Haran G, 2022 *Acc Chem Res* **55**, 1659–1668.
[146] Tan P H, Han W P, Zhao W J, Wu Z H, Chang K, Wang H, Wang Y F, Bonini N, Marzari N, Pugno N, et. al., 2012 *Nat. Mater.* **11** 294-300
[147] Zhang X, Han W P, Wu J B, Milana S, Lu Y, Li Q Q, Ferrari A C and Tan P H, 2013 *Phys. Rev. B* **87** 115413
[148] Pizzi G, Milana S, Ferrari A C, Marzari N and Gibertini M, 2021 *ACS Nano* **15** 12509-1253
[149] Xu C, Zhou G, Alexeev EM, Cadore AR, Paradisanos I, Ott AK, Soavi G, Tongay S, Cerullo G, Ferrari AC et. al., 2023 *ACS Nano* **17**, 16682-16694
[150] Yang J, Lee J U and Cheong H, 2017 *FlatChem* **3** 64-70
[151] Lee J U, Park J, Son Y W and Cheong H, 2015 *Nanoscale* **7** 3229–3236
[152] O'Brien O, McEvoy N, Hanlon D, Hallam T, Coleman J N and Duesberg G S, 2015 *Sci. Rep.* **6** 19476
[153] Shi W, Lin M L, Tan Q H, Qiao X F, Zhang J and Tan P H, 2016 *2D Mater.* **3** 025016
[154] Zhao W, Ghorannevis Z, Chu L, Toh M, Kloc C, Tan P H and Eda G, 2013 *ACS Nano* **7** 791-797
[155] Zhu B, Chen X and Cui Z, 2015 *Sci. Rep.* **5** 9218
[156] Corro E, Botello-Mendez A, Gillet Y, Elias A L, Terrones H, Feng S, Fantini C, Rhodes D, Pradhan N, Balicas L, et.al., 2016 *Nano Lett.* **16** 2363-2368
[157] Zhao Y, Han S, Zhang J and Tong L, 2020 *J. Raman Spectrosc.* **52** 1-7

Accepted Manuscript

[158] Carvalho B R, Malard L M, Alves J M, Fantini C and Pimenta M A, 2015 *Phys. Rev. Lett.* **114** 136403
[159] Carvalho B R and Pimenta M A, 2020 *2D Mater.* **7** 042001
[160] Gontijo R N, Resende G C, Fantini C and Carvalho B R, 2019 *J. Mater. Research* **34** 1976-1992
[161] Carvalho B R, Wang Y, Mignuzzi S, Roy D, Terrones M, Fantini C, Crespi V H, Malard L M and Pimenta M A, 2017 *Nat. Commun.* **8** 14670
[162] Cheiwchanchamnangij T and Lambrecht W R L, 2012 *Phys. Rev. B* **85** 205302
[163] Cardona M, Pinczuk A, Burstein E, Martin R M, Falicov L M, Klein M V, Brodsky M H, Pine A S and Shen Y-R, *Light Scattering in Solids 1* (Max-Planck-Institut für Festkörperforschung, Stuttgart 80, Fed. Rep. of Germany, 1975).
[164] Reich S, Ferrari A C, Arenal R, Loiseau A, Bello I and Robertson J, 2005 *Phys. Rev. B* **71** 205201
[165] Arenal R, Ferrari A C, Reich S, Wirtz L, Mevellec J Y, Lefrant S, Rubio S and Loiseau A, 2006 *Nano Lett.* **6** 1812
[166] Cadore A R, Oliveira R, Longuinhos R, Teixeira V C, Nagaoka D A, Alvarenga V T, Ribeiro-Soares J, Watanabe K, Taniguchi T, Paniago R M, et. al., 2022 *2D Mater.* **9** 035007
[167] Mohiuddin T M G, Lombardo A, Nair R R, Bonetti A, Savini G, Jalil R, Bonini N, Basko D M, Galiotis C, Marzari, N et. al., 2009 *Phys. Rev. B* **79** 205433
[168] Yoon D, Son Y W and Cheong H, 2011 *Phys. Rev. Lett.* **106** 155502
[169] Ferrari A C, Meyer J C, Scardaci V, Casiraghi C, Lazzeri M, Mauri F, Piscanec S, Jiang D, Novoselov K S, Roth S and Geim A K, 2006 *Phys. Rev. Lett.* **97** 187401

Accepted Manuscript